The Astrophysical Journal Letters, 1011:L22 (21pp), 2026 November 1 https://doi.org/10.3847/2041-8213/aea990
© 2026. The Author(s). Published by the American Astronomical Society.
OPEN ACCESS

An Extremely Bright Slow-rising Afterglow from an Off-axis Jet in GRB 260310A

Yu-Han Yang[1], Roberto Ricci[1,2], Eleonora Troja[1], Muskan Yadav[1], Yi-Han Iris Yin[3,4], Rubén Sánchez-Ramírez[5], Brendan O'Connor[6], Niccolò Passaleva[1,7], Alberto J. Castro-Tirado[5,8], Hendrik van Eerten[9], Simone Dichiara[10], Vincenzo Galluzzi[2,11], Narjes Shahamat Dehsorkh[1], Iván Agudo[5], Jesús Aceituno[5], Malte Busmann[12,13], Maria D. Caballero-García[5], Emilio Fernández-García[5], Daniel Gruen[12,13], Maria Gritsevich[5], Sergiy Guziy[5,14], David Hiriart[15], You-Dong Hu[16], Martin Jelínek[17], Alexander Kutyrev[18,19], Alzbeta Malenakova[17], Filip Novotny[17,20], Ignacio Pérez-García[5], Shashi B. Pandey[21], Jorma Ryske[22], Alfredo Sota[5], Jan Strobl[17], Hira Waseem[1,7], and Siyu Wu[5]

[1] Department of Physics, University of Rome "Tor Vergata", via della Ricerca Scientifica 1, I-00133 Rome, Italy; yuhan.yang@roma2.infn.it, eleonora.troja@uniroma2.it
[2] INAF—Istituto di Radioastronomia, via Gobetti 101, I-40129 Bologna, Italy
[3] The Hong Kong Institute for Astronomy and Astrophysics, The University of Hong Kong, Hong Kong, People's Republic of China
[4] Department of Physics, The University of Hong Kong, Pokfulam Road, Hong Kong, People's Republic of China
[5] Instituto de Astrofísica de Andalucía (IAA-CSIC), Glorieta de la Astronomía s/n, 18008 Granada, Spain
[6] McWilliams Center for Cosmology and Astrophysics, Department of Physics, Carnegie Mellon University, Pittsburgh, PA 15213, USA
[7] Department of Physics, University of Rome "Sapienza", P.le Aldo Moro 2, I-00185 Rome, Italy
[8] Ingeniería de Sistemas y Automática, Universidad de Málaga, Unidad Asociada al CSIC por el IAA, Escuela de Ingenierías Industriales, Arquitecto Francisco Peñalosa, 6, Campanillas, 29071, Málaga, Spain
[9] Department of Physics, University of Bath, Building 3 West, Bath BA2 7AY, UK
[10] Department of Astronomy and Astrophysics, The Pennsylvania State University, 525 Davey Lab, University Park, PA 16802, USA
[11] INAF—Italian Centre for Astronomical Archives c/o Osservatorio Astronomico di Trieste, Via Tiepolo 11, I-34143, Trieste, Italy
[12] University Observatory, Faculty of Physics, Ludwig-Maximilians-Universität München, Scheinerstr. 1, 81679 Munich, Germany
[13] Excellence Cluster ORIGINS, Boltzmannstr. 2, 85748 Garching, Germany
[14] Petro Mohyla Black Sea National University, Mykolaiv 54000, Ukraine
[15] Instituto de Astronomía, Universidad Nacional Autónoma de México (IA-UNAM), carretera Tijuana-Ensenada, km. 107, C.P. 22860 Ensenada, Baja California, México
[16] Guangxi Key Laboratory for Relativistic Astrophysics, School of Physical Science and Technology, Guangxi University, Nanning 530004, People's Republic of China
[17] Astronomical Institute, Czech Academy of Sciences, Fričova 298, 251 65 Ondřejov, Czechia
[18] Astrophysics Science Division, NASA Goddard Space Flight Center, 8800 Greenbelt Rd., Greenbelt, MD 20771, USA
[19] Department of Astronomy, University of Maryland, College Park, MD 20742-4111, USA
[20] Masaryk University Brno, Faculty of Natural Sciences, Kotlářská 2, 602 00 Brno, Czechia
[21] Aryabhatta Research Institute of Observational Sciences (ARIES), Manora Peak, Nainital, Uttarakhand 263001, India
[22] URSA Astronomical Association, Kopernikuksentie 1, 00130 Helsinki, Finland
Received 2026 May 25; revised 2026 August 2; accepted 2026 August 13; published 2026 October 28

Abstract

We present a multiwavelength study of GRB 260310A, a nearby long-duration gamma-ray burst (GRB) at $z \simeq 0.153$ associated with a broad-lined Type Ic supernova. Despite its modest prompt gamma-ray output, $E_{\gamma,\mathrm{iso}} \simeq 3.5 \times 10^{50}$ erg, GRB 260310A exhibits one of the brightest afterglows ever observed in the X-ray, optical, and radio bands. Its apparent brightness is not its only remarkable feature. The optical afterglow displays a delayed onset, characterized by a slow rising phase, with slope $\alpha \approx -1$, and a late peak at $\sim$0.1 day. We argue that the combination of weak prompt emission, hard peak energy, and late afterglow onset is naturally explained by a GRB jet viewed off-axis. The radio spectral energy distributions are consistent with synchrotron radiation and indicate the presence of both reverse- shock (RS) and forward-shock (FS) components, thus providing a first test of RS models in an off-axis geometry. The X-ray afterglow displays a prominent rebrightening, monitored for up to $\sim$68 days with no evidence of spectral evolution. A low level of linear polarization, $\Pi \approx 1.7\%$, is measured at 15 GHz at $T_0 + 55$ days and suggests that, at these late times, the FS is the dominant emission component from radio to X-rays. This late-time rebrightening represents a critical test for the two-component jet model. If interpreted as the emergence of a narrow jet core viewed further off-axis, it would imply extreme luminosities and energetics for an on-axis observer.

Unified Astronomy Thesaurus concepts: Time domain astronomy (2109); Gamma-ray bursts (629); Relativistic jets (1390); Core-collapse supernovae (304); Type Ic supernovae (1730)

Materials only available in the online version of record: machine-readable table

1. Introduction

Gamma-ray bursts (GRBs) are among the brightest and most energetic explosions in the Universe (B. Zhang & P. Mészáros 2004; T. Piran 2004; N. Gehrels & P. Mészáros 2012). Detected as brief flashes of gamma rays from cosmological distances, they are followed by a longer-lasting afterglow

Original content from this work may be used under the terms of the Creative Commons Attribution 4.0 licence. Any further distribution of this work must maintain attribution to the author(s) and the title of the work, journal citation and DOI.

visible across the electromagnetic spectrum, from X-rays to radio wavelengths (E. Costa et al. 1997; J. van Paradijs et al. 1997; D. A. Frail et al. 1997). Their extreme luminosities are powered by a central compact object—either an accreting black hole (R. Narayan et al. 1992) or a massive neutron star (V. V. Usov 1992)—driving an ultrarelativistic jet (J. E. Rhoads 1999; R. Sari et al. 1999).

Most GRBs detected to date are those whose jets are closely aligned with our line of sight (on-axis), so that their emission is strongly Doppler-boosted and easily detectable. As a result, on-axis observers probe only the inner and most energetic portion of the outflow (jet core), while remaining largely insensitive to the angular structure at wider angles (J. Granot et al. 2002; E. Rossi et al. 2002; B. Zhang & P. Mészáros 2002a). Any stratification in energy and Lorentz factor outside the core, as well as the presence of a cocoon or slower wings (E. Ramirez-Ruiz et al. 2002; E. Nakar & T. Piran 2017; L. Izzo et al. 2019), is essentially hidden from view. In this sense, standard on-axis GRBs provide an incomplete picture of the jet, which can often be approximated as a simple "top hat" even when the outflow is intrinsically structured.

However, the majority of GRB jets are oriented away from the observer (Y. F. Huang et al. 2002; J. Granot et al. 2002; G. Ryan et al. 2015; S. P. Chakyar & L. Resmi 2025) and remain largely unseen. As the viewing angle increases, relativistic beaming reduces both the observed flux and the characteristic photon energies, causing these events to fall below the sensitivity thresholds of traditional gamma-ray detectors. Thus, GRBs seen off-axis are expected to manifest as weak high-energy transients, or even gamma-ray dark events (J. E. Rhoads 1999; R. Yamazaki et al. 2003; D. Lazzati et al. 2017; F. Xu et al. 2023; J.-H. Zheng & W. Lu 2026), whose multiwavelength afterglows evolve on longer timescales compared to classical on-axis bursts (J. Granot et al. 2002; H. van Eerten & A. MacFadyen 2013; A. Kathirgamaraju et al. 2018; G. Ryan et al. 2020). Uncovering this population of misaligned jets is essential to provide a complete census of relativistic explosions and constrain their jet structure, which encodes unique information about their progenitors and jet launching mechanisms (H. Nagakura et al. 2014; D. Lazzati et al. 2017; G. Urrutia et al. 2021; O. Gottlieb et al. 2021; O. Gottlieb & E. Nakar 2022; B. O'Connor et al. 2023).

A breakthrough came with the discovery of GRB 170817A, the first binary neutron star merger detected via gravitational waves and electromagnetic radiation (B. P. Abbott et al. 2017). Unlike classical GRBs, this event was observed significantly off-axis, providing an unprecedented view of a relativistic jet from outside its core. The prompt gamma-ray signal was underluminous compared to typical short GRBs (A. Goldstein et al. 2017; B.-B. Zhang et al. 2018a), while the afterglow exhibited a delayed rise (E. Troja et al. 2017; G. Hallinan et al. 2017) and a long-lived evolution (K. P. Mooley et al. 2018; E. Troja et al. 2018a; D. Lazzati et al. 2018; R. Margutti et al. 2018; G. P. Lamb et al. 2019; E. Troja et al. 2019, 2020; A. Balasubramanian et al. 2022; G. Ryan et al. 2024)—hallmarks of an off-axis jet. This provided the clearest observational evidence to date that GRB jets are not simple top-hat outflows, but instead possess an angular structure shaped by their interaction with the surrounding ejecta.

Besides the case of GRB 170817A, structured or two-component jets—consisting of a narrow ultrarelativistic core surrounded by a wider, slower outflow—have been investigated to explain the complexity of some GRB afterglows (K. Sheth et al. 2003; F. Peng et al. 2005; J. L. Racusin et al. 2008; B. O'Connor et al. 2023; Y. Sato et al. 2025), whereas the off-axis scenario was discussed to explain the peculiar behavior of some nearby and underluminous GRBs such as, for example, GRB 980425 (T. J. Galama et al. 1998a; R. Yamazaki et al. 2003), GRB 031203 (E. Ramirez-Ruiz et al. 2005), and GRB 171205A (V. D'Elia et al. 2018). However, the nature of these nearby subenergetic bursts remains debated. In particular, it is still unclear whether they represent classical GRBs viewed off-axis or instead arise from a distinct population powered by a different central engine and involving mildly relativistic quasi-isotropic outflows (A. M. Soderberg et al. 2006; E. Liang et al. 2007; D. Guetta & M. Della Valle 2007; F. J. Virgili et al. 2009; F. Xu et al. 2023).

In this context, the recent GRB 260310A is a particularly informative case. This burst, discovered by the Gamma-ray Burst Monitor (GBM; C. Meegan et al. 2009) on board Fermi (Fermi GBM team 2026), was successfully localized by wide-field optical monitors (D. O'Neill et al. 2026; R. L. Becerra et al. 2026) thanks to its delayed bright afterglow peak. Subsequent observations at X-ray, optical, and radio wavelengths single it out as one of the brightest GRB afterglows detected thus far (D. A. Perley et al. 2026). The burst was initially proposed as a possible merger-driven long burst (N. Gehrels et al. 2006; J. C. Rastinejad et al. 2022; J. Yang et al. 2022; E. Troja et al. 2022; Y.-H. Yang et al. 2024) due to its deviation from the canonical Amati relation (L. Amati et al. 2002; J.-L. Atteia et al. 2026) and large Galactocentric offset (J. S. Bloom et al. 2002; W.-F. Fong et al. 2022; B. O'Connor et al. 2022). However, despite these shared properties, GRB 260310A has ultimately been identified as a standard long GRB followed by a broad-lined supernova (SN) at $z \approx 0.153$ (A. de Ugarte Postigo et al. 2026; B. O'Connor et al. 2026b).

In this Letter, we present the results of our multiwavelength follow-up observations, spanning ~60 days after the burst. Our dataset comprises extensive optical and near-infrared (NIR) observations obtained with multiple facilities, radio observations with the Karl G. Jansky Very Large Array (VLA), together with X-ray monitoring by the Follow-up X-ray Telescope (FXT) on board the Einstein Probe (EP), Chandra, XMM-Newton, and the Nuclear Spectroscopic Telescope Array (NuSTAR), tracing one of the brightest X-ray afterglows ever observed.

Throughout the manuscript, we adopt a standard ΛCDM cosmology (Planck Collaboration et al. 2020) with $H_0 = 67.4\,\mathrm{km\,s^{-1}\,Mpc^{-1}}$, $\Omega_\mathrm{m} = 0.315$, and $\Omega_\Lambda = 0.685$. All the errors and upper limits are reported at the 1σ and 3σ confidence levels, respectively.

2. Observation and Data Reduction

2.1. Gamma Rays

At UT 04:57:10 on 2026, March 10 (hereafter T_0), GRB 260310A was triggered by the Fermi GBM with an on-ground calculated location at R.A. = 213.°6, decl. = 78.°7 with a statistical uncertainty of 4.°3 (Fermi GBM team 2026). From the 12 NaI and two BGO detectors on board, we selected detectors na, nb, and b1, which provide the smallest viewing angles relative to the GRB source direction. The time-tagged event data were retrieved and reduced with `heapy`.[23] The

[23] https://github.com/jyangch/heapy

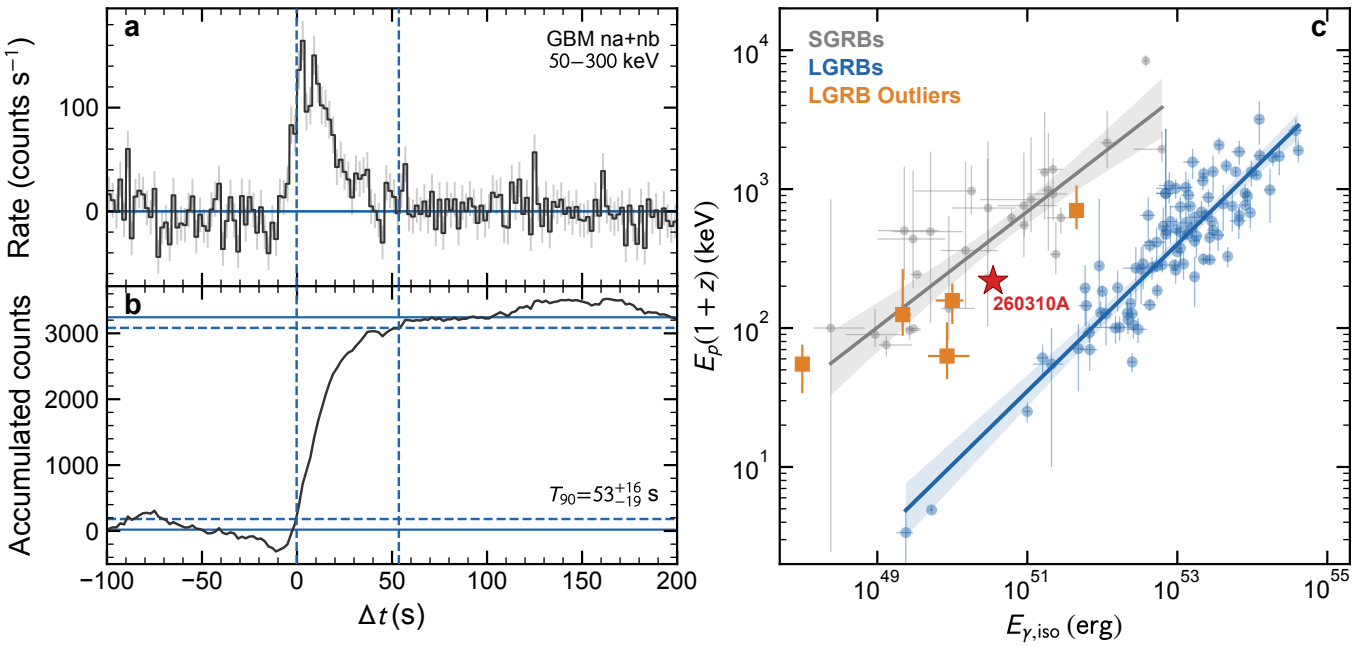


Figure 1. Prompt emission properties of GRB 260310A. (a). Fermi/GBM count-rate light curves from NaI detectors na and nb in the 50–300 keV energy band. The black lines and gray lines represent the net counts and errors with a bin size of 2 s. (b). Accumulated counts. The blue horizontal solid (dashed) lines are drawn at 0%–100% (5%–95%) of the total accumulated counts. The vertical lines in (a) and (b) represent the T_{90} interval. (c). Amati relation diagram (L. Amati et al. 2002; B.-B. Zhang et al. 2018a, 2018b). Type I (short) and Type II (long) GRBs are shown as gray and blue circles, and the corresponding solid lines and dashed regions are the best-fit models and 95% c.l., respectively. The red star marks the position of GRB 260310A. Other outliers (GRBs 980425, 031203, 061021, 161219B, and 171205A) are marked as orange squares.

combined na and nb light curve of GRB 260310A (Figure 1, left panel) in the energy range of 50–300 keV exhibits a pulse with a fast-rise and exponential-decay profile, with a measured burst duration $T_{90} = 53^{+16}_{-19}$ s. The minimum variability timescale (V. Z. Golkhou & N. R. Butler 2014; V. Z. Golkhou et al. 2015) is only loosely constrained to $\Delta t_{\rm min} < 5$ s.

We conducted a time-integrated spectral fitting using na, nb, and b1 data covering the T_{90} time interval. The spectrum is well described by a cutoff power-law model with photon index of -0.2 ± 0.3 and peak energy of $E_{\rm p} = 157^{+15}_{-13}$ keV. The derived fluence is $5.2^{+0.6}_{-0.3} \times 10^{-6}$ erg cm^{-2} (10–1000 keV), yielding a rest-frame isotropic-equivalent energy of $E_{\gamma,\rm iso} = 3.5^{+0.4}_{-0.2} \times 10^{50}$ erg. The derived peak flux and rest-frame peak luminosity in the time interval of $[T_0,\ T_0 + 2\,{\rm s}]$ are $2.3^{+0.6}_{-0.4} \times 10^{-7}$ erg cm^{-2} s^{-1} and $L_{\gamma,\rm pk} = 1.5^{+0.4}_{-0.3} \times 10^{49}$ erg s^{-1}. The location of GRB 260310A in the Amati diagram (L. Amati et al. 2002) is shown in Figure 1(c).

2.2. X-Rays

2.2.1. EP

The position of GRB 260310A was not covered by the Wide-field X-ray Telescope on board EP within a time window of $T_0 \pm 1$ hr around the GBM trigger.

The FXT on board EP began follow-up observations of the field at UT 2026 March 12 17:50:08 ($\Delta t = 2.5$ days). An uncatalogued X-ray source was detected at R.A. = 219.°3152, decl. = 71.°8417 (J2000) with an uncertainty of 10″ in radius (90% confidence level; R. Jayaraman et al. 2026). We further observed it through ToO requests (PIs: Yang, Jayaraman, Xu, Ghirlanda) for 19 epochs that spanned from 2026 March 14 to April 25. All observations were conducted with a thin filter in full frame mode. The FXT data were processed using FXTDAS v1.30, using the latest FXT calibration database (CALDB v1.30). Source photons were extracted from a circle with a radius of 60″ while background photons were extracted from an annulus with radii of 200″–400″.

The resulting X-ray light curve is shown in Figure 2. We describe the afterglow temporal evolution with a smoothly broken power law composed of $n = 4$ segments, defined as

$$F(t) = F_0 t^{-\alpha_1} \prod_{k=1}^{n} \left[1 + \left(\frac{t}{t_{b,k}}\right)^{s}\right]^{-\Delta\alpha_k/s}, \quad (1)$$

where α_k are the slopes, $\Delta\alpha_k = \alpha_{k+1} - \alpha_k$, $t_{b,k}$ are the three temporal break times, and s is a smoothness parameter that controls the sharpness of the transitions. Log-uniform priors were adopted for the flux normalization parameter F_0 and temporal breaks of $t_{b,k} \in [1, 70]$ days, with $t_{b,1} < t_{b,2} < t_{b,3}$ enforced. Uniform priors are used for decay indices $\alpha_k \in [-5, 5]$ and smoothness parameter $s \in [1, 50]$. Parameter estimation was performed with the nested-sampling algorithm via the Python package PyMultiNest (J. Buchner et al. 2014, used hereafter unless otherwise specified). The light curve (Figure 2) exhibits a shallow decay with $\alpha_{X,1} = 0.34 \pm 0.06$, followed by a steep decline with $\alpha_{X,2} = 2.5^{+1.4}_{-0.6}$ after $t_{b,1} = T_0 + 9.1^{+1.2}_{-0.8}$ d. Between $t_{b,2} = T_0 + 18 \pm 2$ days and $t_{b,3} = T_0 + 30 \pm 3$ days, a bump is visible with a slope of $\alpha_{X,3} = -1.2^{+0.9}_{-2.0}$, which subsequently fades with $\alpha_{X,4} = 2.1^{+0.4}_{-0.3}$.

2.2.2. Chandra X-Ray Observatory

To elucidate the origin of the late-time rebrightening visible in the EP light curve (Figure 2), we initiated a Director's Discretionary Time (DDT) Target of Opportunity (ToO)

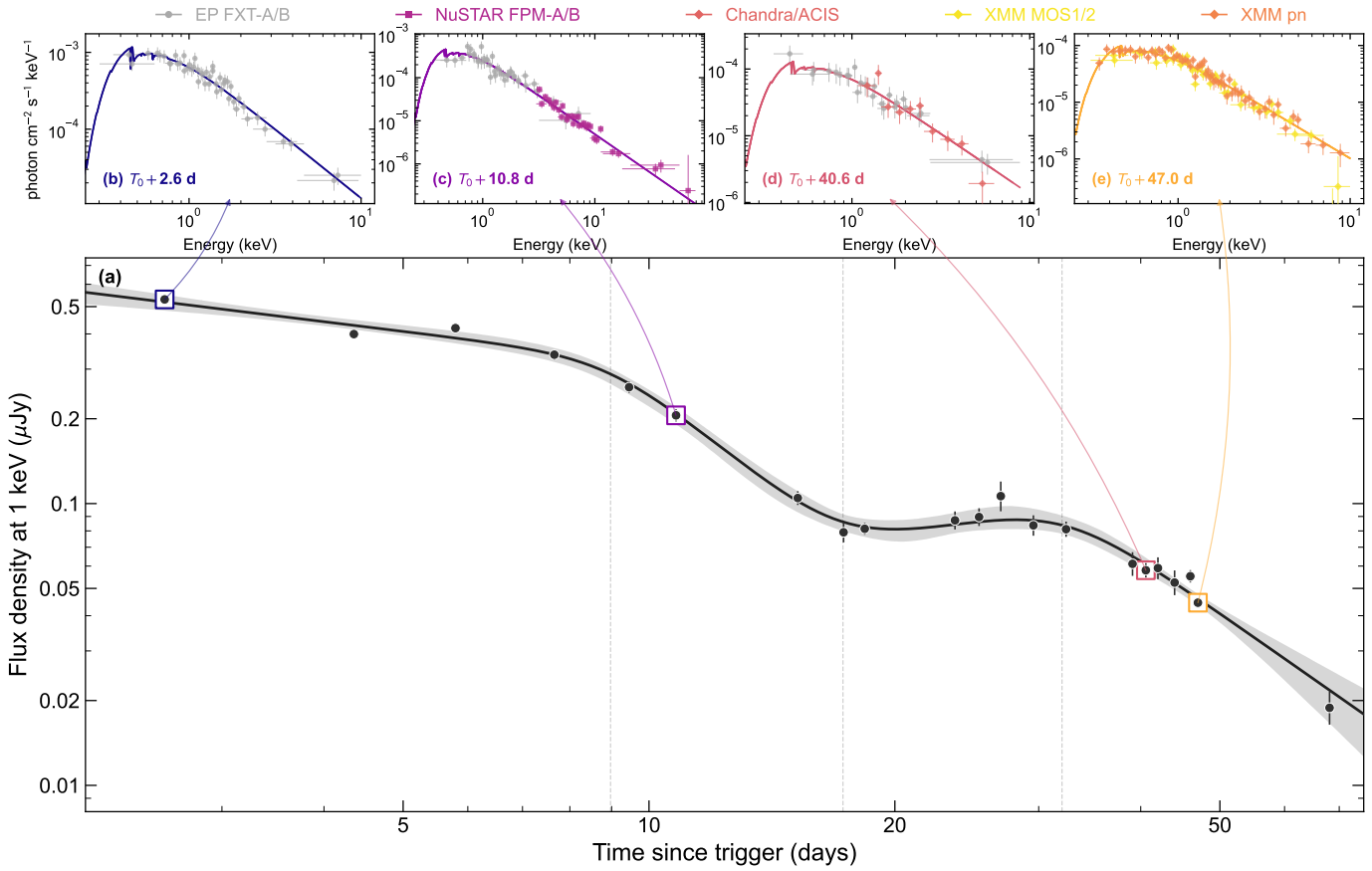


Figure 2. X-ray observations of GRB 260310A. (a). 1 keV flux density light curve fitted with a four-segment smoothly broken power-law model (black solid line) and the associated 95% confidence region (gray shaded area). Vertical dashed lines indicate the break times. Detailed spectral views of four representative epochs: (b) T_0 + 2.6 days (the initial EP/FXT epoch), (c) T_0 + 10.8 days (the first NuSTAR epoch with quasi-simultaneous FXT observations), (d) T_0 + 40.9 days (the Chandra epoch with quasi-simultaneous FXT observations), and (e) T_0 + 47 days (the XMM-Newton epoch). The first six epochs (Interval 1) and the remaining epochs are joint-fitted using a tied intrinsic absorption and a shared photon index within each respective interval. Solid lines in the spectral panels illustrate the best-fit model for each epoch. Spectral fitting was performed on data grouped to $\geqslant$1 count per bin using the C-statistic, and data are rebinned for display purposes.

observation with the Chandra X-ray Observatory. Thanks to its superb angular resolution, only Chandra can assess whether the X-ray measurements are contaminated by a nearby source (Figure 3), unresolved within the EP/FXT's broader point-spread function.

The observation (ObsID: 32306; PI: Yang) was performed at $\approx T_0 + 41$ days with the Advanced CCD Imaging Spectrometer (ACIS), with the target positioned on the back-illuminated S3 chip. The data reduction was carried out using the Chandra Interactive Analysis of Observations (CIAO) v4.18 software (A. Fruscione et al. 2006) and the corresponding calibration database (`CALDB` v4.12.3). Level 2 event files were reprocessed using the `chandra_repro` pipeline and cleaned of periods of elevated background. After standard filtering, the total cleaned exposure time amounts to ∼5 ks. The absolute astrometry was corrected using `fine_astro`, crossmatched against the Gaia DR3 catalog (Gaia Collaboration et al. 2023).

Chandra imaging identifies the GRB afterglow as the dominant contributor to the total flux, and two other weaker sources detected within a 1′ circular region (Y.-H. Yang et al. 2026). This confirms that the observed X-ray rebrightening is an intrinsic feature of the GRB afterglow.

An additional Chandra observation (ObsID: 32337; PI: Jayaraman) was carried out at T_0 + 68 days for an exposure time of ∼10 ks. The data were processed following the same reduction procedure described above. Spectra are extracted via `srcflux` using a 1″ circular region for the source, and a concentric 15″–30″ annulus for the background.

2.2.3. XMM-Newton

After establishing that the late-time X-ray rebrightening is related to the GRB, we initiated a DDT ToO observation with XMM-Newton (ObsID: 0974792201; PI: Yang) to constrain its late-time decay and spectral shape. The target was observed on April 26, 2026 (T_0 + 47 d) using the three detectors (pn, MOS1, and MOS2) on the EPIC in full window mode, with the thin optical-blocking filter. XMM-Newton data were reduced by the Science Analysis System (`SAS`) v22.1 with the most recent calibration files. The exposure times, excluding high-rate flaring particle background, are 16 ks and 20 ks for the pn and MOS detectors, respectively. Source spectra were extracted using a 15″ circular region centered at the GRB coordinates, and the background was obtained using a 60″–100″ annulus for both MOS detectors and a nearby source-free 40″ circle for the pn detector.

2.2.4. NuSTAR

NuSTAR (F. A. Harrison et al. 2013) observed GRB 260310A at two epochs (T_0 + 10.7 days and T_0 + 32.4 days) through a DDT ToO request (ObsIDs: 91202417002, 91202417004; PI: Waratkar). The preliminary results of these observations

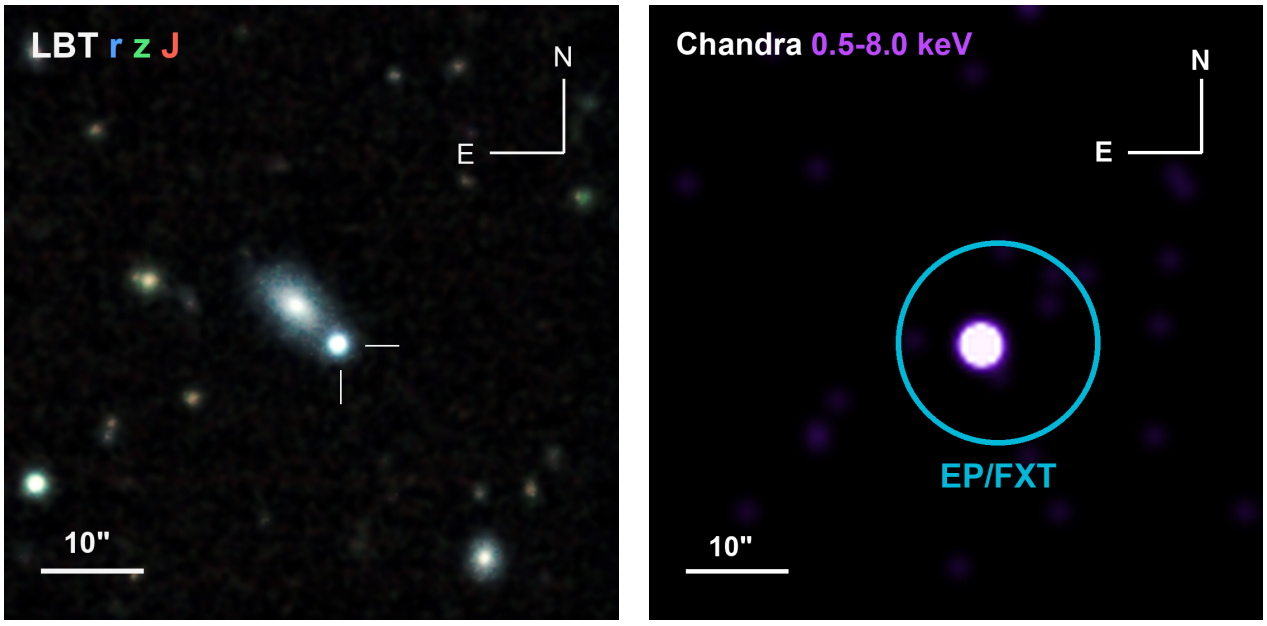


Figure 3. Left panel: false-color LBT image of the field of GRB 260310A, constructed from the *r*, *z*, and *J* bands, mapped to blue, green, and red, respectively. The transient position is marked by white ticks. Right panel: 0.5–8.0 keV Chandra image of the same field, smoothed with a Gaussian kernel of $\sigma = 2$ pixels. The cyan circle marks the EP/FXT localization region. In both panels, north is up, east is to the left, and the scale bar is 10″.

(E. Kammoun et al. 2026; G. Waratkar et al. 2026) report the detection of an X-ray counterpart in both epochs.

The NuSTAR data were reduced using the standard tasks in the NuSTARDAS pipeline, distributed as part of `HEASoft` v6.34. We extracted the source and background spectra using `nuproducts` from a 50″ circular region and a 120″–200″ annulus centered on the source, respectively, for both FPMA and FPMB.

2.2.5. X-Ray Spectral Analysis

Motivated by the changes in temporal behavior (Section 2.2.1), we divided the X-ray observations into two temporal intervals and analyzed them independently. Interval 1 covers the period from $T_0 + 2.6$ days to $T_0 + 11$ days and includes the first six FXT epochs together with the first NuSTAR epoch, while interval 2 spans from $T_0 + 15$ days to $T_0 + 47$ days and comprises the remaining FXT epochs, the Chandra and XMM-Newton observations, as well as the second NuSTAR epoch.

The X-ray spectra, obtained with FXT (0.3–10 keV), Chandra (0.5–8 keV), NuSTAR (3–79 keV), and XMM-Newton (0.3–10 keV) were fitted using the `XSPEC` v12.15 (K. A. Arnaud 1996) with an absorbed power-law model considering a Galactic hydrogen column density of $N_{\rm H} = 2.59 \times 10^{20}$ cm^{-2} (R. Willingale et al. 2013) and the intrinsic absorption $N_{\rm H,z}$ from the GRB site (`tbabs*ztbabs*powerlaw`; J. Wilms et al. 2000). The spectra are well fit with a common $N_{\rm H,z} = (1.6 \pm 0.2) \times 10^{21}$ cm^{-2} and consistent photon indices $\Gamma = 1.80 \pm 0.04$ (interval 1) and $\Gamma = 1.82 \pm 0.05$ (interval 2),[24] indicating no evidence for spectral variation within the uncertainties.

Our results differ from the preliminary report of R. Jayaraman et al. (2026) with $\Gamma \approx 1.55$. This discrepancy can be explained by the different absorption model adopted in R. Jayaraman et al. (2026), which reports only a fixed Galactic hydrogen column density, whereas our fit includes both Galactic and intrinsic absorption components.

The unabsorbed flux in the 0.3–10 keV band and the flux density at 1 keV (with the 3–79 keV fluxes and 10 keV flux density additionally reported for NuSTAR), derived from these best-fit models, are listed in Table A1 and shown in Figure 2.

2.3. Optical and NIR Imaging

We carried out imaging observations of the field of GRB 260310A across a broad range of optical and NIR bands using multiple facilities: the Burst Observer and Optical Transient Exploring System (BOOTES; A. J. Castro-Tirado 2023; Y.-D. Hu et al. 2023), the Observatorio de Sierra Nevada (OSN), the Large Binocular Telescope (LBT), the Ondřejov observatory, and the Optical Monitor (OM) on board XMM-Newton.

The transient is located in the outskirts of a bright galaxy (Figure 3), whose diffuse light partially affects the target's photometry. Archival *grz*-band images from the DESI Legacy Imaging Surveys (A. Dey et al. 2019) and *i*-band images from the Pan-STARRS Surveys (K. C. Chambers et al. 2016; E. A. Magnier et al. 2020) served as reference templates. Unless otherwise specified, aperture photometry for the optical and NIR imaging was calibrated against the ATLAS All-Sky Stellar Reference Catalog (Refcat2; J. L. Tonry et al. 2018) and the Two Micron All Sky Survey (2MASS; M. F. Skrutskie et al. 2006) catalog, respectively. Further details are provided in the Appendix. The photometric results for the complete dataset, including supplementary optical/NIR data obtained from public archives, are presented in Table A1. Additional optical/NIR data from B. O'Connor et al. (2026a) were also incorporated into the analysis. Galactic extinction corrections were applied to the entire dataset prior to model fitting using the `G23` extinction curve model (K. D. Gordon et al. 2023, see also K. D. Gordon et al. 2009; E. L. Fitzpatrick et al. 2019; K. D. Gordon et al. 2021, and M. Decleir et al. 2022), adopting

[24] Uncertainties are quoted for the joint 1σ confidence regions for the three parameters (M. Lampton et al. 1976), accounting for the inherent correlations among them.

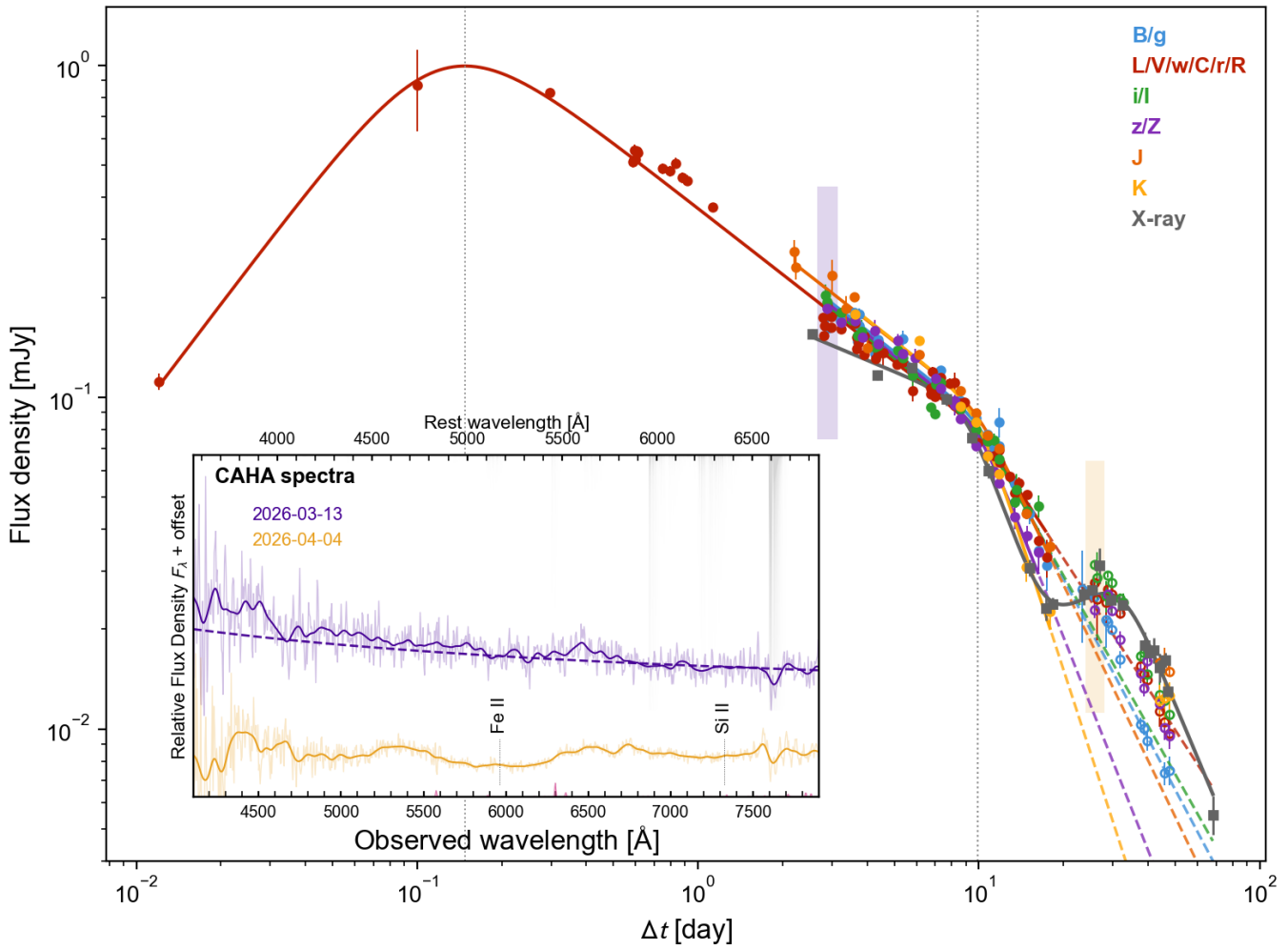


Figure 4. Multicolor optical and NIR light curves of GRB 260310A, compared to the X-ray light curve (gray squares). Data were rescaled to the *R* band assuming $F_\nu \propto \nu^{-\beta}$ with $\beta = 0.91$. The absolute X-ray flux is shown in Figure 2(a). The red solid line shows the best-fit temporal model, describing the early optical data. Dashed lines show the late-time decay in different colors. Vertical bars mark the two epochs of optical spectroscopy. Inset: CAHA spectra observed on 2026, March 13 and April 4, corrected for Galactic extinction. To guide the eye, the dashed line shows a power-law spectrum with slope 0.91. The observed spectra are plotted as semi-transparent lines, with smoothed solid lines for plotting purposes. Smoothing is performed using a Gaussian kernel with a standard deviation of 5 pixels. Wavelengths affected by telluric absorption and sky emission are marked by gray and pink areas, respectively (S. D. Lord 1992).

$R_V = 3.1$ and $A_V = 0.058$ from the Gaia Total Galactic Extinction (TGE) map (L. Delchambre et al. 2023).

After excluding the rebrightening at >20 days, we fitted the optical/NIR light curves with a smoothly broken power-law model (Equation (1)) composed of $n = 3$ segments. The first two temporal slopes were tied across all bands, while the third slope was allowed to vary independently. A systematic uncertainty of 5% was added in quadrature to the photometric errors. We fixed the smoothness parameter to a relatively soft value of $s = 3$ for the first break, which provides a better representation of the broad optical peak, while a sharp $s = 10$ was used for the latter break to better constrain the slopes. The data and best-fit light curves, normalized to the *R* band, are shown in Figure 4. The optical/NIR emission initially rises with a temporal slope of $\alpha_1 \approx -1$ up to ∼0.1 day, followed by a shallower decay with $\alpha_2 = 0.67 \pm 0.01$. At ∼9 days, the light curves exhibit an achromatic break, also visible at X-ray energies. After this time, the flux decays at a faster rate with a slope that varies among different bands, as also found by B. O'Connor et al. (2026a). We derive $\alpha_3 = 1.7 \pm 0.2$ for g/B, 1.4 ± 0.1 for $L/V/w/C/r/R$, 1.5 ± 0.2 for i/I, 2.2 ± 0.2 for z/Z, 1.9 ± 0.2 for *J*, and 2.8 ± 0.3 for the *K* bands. This chromatic behavior is likely due to the SN onset (B. O'Connor et al. 2026a).

2.3.1. Dust Extinction

Dust extinction alters the afterglow spectrum, introducing curvature relative to the intrinsic power-law shape. To decouple the intrinsic optical/NIR spectral index from dust-induced curvature, we model the afterglow emission as $F_\nu(\nu, t) \propto \nu^{-\beta} t^{-\alpha}$, introducing an extinction component parameterized by the reddening $E(B-V)_z$. We jointly fit the host-subtracted optical and NIR data (from this work, supplemented by B. O'Connor et al. 2026a) spanning $T_0 + 2$ days to $T_0 + 6$ days, during which no significant spectral or temporal breaks are observed. All measurements were first corrected for Galactic extinction. The intrinsic dust extinction is modeled using the `G23` extinction curve with $R_V = 3.1$. Uniform priors are assigned to α, β, and $E(B-V)_z$, and a log-uniform prior to the normalization. The fit constrains $\alpha = 0.65 \pm 0.05$ and $\beta_O = 0.91^{+0.06}_{-0.09}$ with reddening

$E(B-V)_z = 0.02^{+0.03}_{-0.01}$, indicating a dust-poor local environment, consistent with the large Galactocentric offset of the transient.

When compared with the absorption column inferred from X-ray spectroscopy, the derived extinction implies a high gas-to-dust ratio, $N_{\mathrm{H},z}/A_V \approx 2.5 \times 10^{22}\,\mathrm{cm}^{-2}\,\mathrm{mag}^{-1}$, an order of magnitude higher than in the Milky Way. This is consistent with the well-known trend of GRB sightlines showing large X-ray columns and modest optical reddening (G. Stratta et al. 2004).

2.3.2. Optical Polarimetry

We conducted optical polarimetry with the DIPOL instrument installed at the 90 cm telescope (T90) in Observatorio de Sierra Nevada (Granada, Spain) in two epochs during the night of March 12 and March 13 (16×300 s each). Data were reduced using the Interactive Optical Photo-Polarimetric Python Pipeline (J. Escudero Pedrosa et al. 2024). Resulting polarization was $2\% \pm 2\%$ and $4\% \pm 2\%$, respectively, consistent with null polarization and in agreement with the 3σ upper limit of $<1.5\%$ reported at a similar epoch (M. Pursiainen et al. 2026).

2.4. Optical Spectroscopy

Spectroscopic observations were carried out with the 2.2 m Calar Alto Faint Object Spectrograph mounted on the 2.2 m telescope at Calar Alto Observatory (CAHA), Spain, on 2026 March 13 ($T_0 + 2.9$ days) and April 4 ($T_0 + 26$ days) under Program 26A-2.2-026 (PI: A. J. Castro-Tirado). Exposure times were 400 s and 3×900 s for the two epochs, respectively. The observations employed a 2.9″ slit together with the g200 grism, providing wavelength coverage over 4000–8000 Å. The first epoch was obtained under poor seeing and high-humidity conditions, while the second epoch was conducted under improved conditions, with a seeing of 1.2″. The data were reduced following standard `IRAF` procedures, including bias, flat, wavelength, and flux calibrations. The reduced spectra are shown in the inset of Figure 4. In the first epoch, the spectrum displays a featureless power-law continuum consistent with afterglow-dominated emission. By the second epoch, the spectrum reveals the emergence of broad undulations. These spectral features are typical of broad-lined Type Ic supernovae, in which high ejecta expansion velocities broaden and blend atomic transitions (M. Modjaz et al. 2016).

Two broad bumps are visible around rest-frame 4600 and 5800 Å. The ∼4600 Å rest-frame peak is dominated by the blended emission of Fe II multiplets, while the adjacent dips are formed by the strongly blueshifted, broad absorption components of Fe II λ5169 and Si II λ6355.

Although the optical and X-ray light curves exhibit a rebrightening on comparable timescales (Figure 4), their spectral properties are markedly different and point to distinct emission components. Our spectral analysis of the X-ray rebrightening shows that it is well described by a nonthermal power-law spectrum (Figure 2). In contrast, the optical rebrightening is spectroscopically classified as a Type Ic supernova. This implies that the power-law component responsible for the X-ray rebrightening becomes subdominant in the optical band.

2.5. Radio

Observations with the Karl G. Jansky VLA in the A-array were initiated on 2026 March 18 ($T_0 + 8.2$ days), under project No. 26A-516 (PI: Troja) in the *C* band with central frequencies of 6 GHz and corresponding bandwidths of 4 GHz. After the association with an SN became apparent, observations continued under Director's Discretionary Time (DDT; PI: D. Perley) and were publicly released. The flux, bandpass, and polarization angle (PA) calibrator was 3C286; the phase calibrators were J1531+7206 and J1357+7643, respectively.

Data were retrieved from the National Radio Astronomy Observatory online archive and flagged, calibrated, and imaged in Common Astronomy Software Applications (CASA v6.6.1; CASA Team et al. 2022) using standard procedures. The imaging was performed with the `TCLEAN` task using a Briggs parameter of 0.5. The `IMSTAT` task was used to evaluate rms noise in a region of the restored map away from bright side-sources. A 2D Gaussian fit was performed inside the `viewer` task. The peak fluxes and the corresponding 1σ uncertainties are reported in Table A1, and are consistent with those reported in the gamma-ray coordinates (D. A. Perley et al. 2026; G. Schroeder et al. 2026).

2.5.1. Radio Polarimetry

Given the brightness of its radio counterpart, GRB 260310A was an excellent target for polarization studies (e.g., C. T. Christy et al. 2026). Unfortunately, the scheduling blocks discussed above relied on a polarized phase calibrator observed over a limited range of parallactic angles. Such a setup does not allow us to estimate the instrumental leakage terms (D-terms) necessary for a reliable calibration of the polarization vectors.

To recover a polarization model for the phase calibrator, we reobserved GRB 260310A with the VLA on May 5 in the Ku band ($T_0 + 55$ days) and on May 17 in the *C* and *X* bands ($T_0 + 68$ days), adding an unpolarized calibrator (J1407+2827) to the schedule.

We followed the standard polarization calibration steps: (1) setting the polarization model for the primary calibrator 3C286 (R. A. Perley & B. J. Butler 2017); (2) correcting for cross-hand (R-L, L-R) delays to ensure phases are aligned using 3C286; (3) solving for instrumental leakage terms (D-terms) using the unpolarized calibrator J1407+2827; (4) solving for the R-L polarization phase difference using 3C286. The calibration solutions were then applied to the phase calibrator J1357+7643 and the GRB.

The polarization-calibrated data of the primary calibrator, phase calibrator and target were imaged using `TCLEAN` with all four Stokes parameters (I, Q, U, V) using a Briggs parameter of 0.5. The I-, Q-, and U-Stokes Ku-band (15 GHz) images are shown in Figure 5. From the Q- and U-Stokes maps, the debiased linear polarization intensity was derived as $P = \sqrt{Q^2 + U^2 - \sigma_Q^2}$ (J. F. C. Wardle & P. P. Kronberg 1974), where Q and U are measured at the position of the flux peak, and σ^2 is the image rms. The fractional polarization was then derived as $\Pi = P/I$, where I is the peak flux density of total intensity (Stokes I). The PA was calculated as $\chi = 0.5 \tan^{-1}(U/Q)$. The leakage terms calibrator showed a polarization fraction below 1%, and the phase calibrator J1357+7643 was polarized at a level of $\Pi = 4.1\% \pm 0.2\%$ with PA $= 29.^{\circ}2 \pm 1.^{\circ}4$. For the target, we measure a polarization

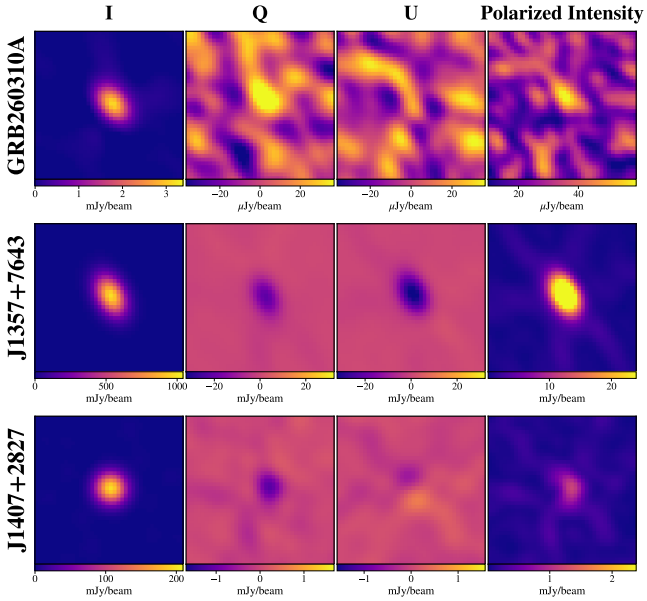


Figure 5. Stokes *I, Q, U* images and linear polarization map for the target GRB 260310A (top), the phase calibrator J+1357 (middle) and the leakage term calibrator J+1407 (bottom). The field was imaged at $T_0 + 55$ days in the Ku band.

fraction $\Pi = 1.7\% \pm 0.4\%$ and derive an upper limit of $|\mathrm{PA}| < 18°$. Uncertainties were computed by summing in quadrature a systematic term of 5% of the *I*-, *Q*-, and *U*-Stokes peak flux values with the statistical term. At lower frequencies we derive 3σ upper limits $\Pi_{6\mathrm{GHz}} < 1.7\%$ and $\Pi_{10\mathrm{GHz}} < 2.5\%$.

The polarization model of J1357+7643 was then applied to the entire dataset using the standard pipeline with the `Df+X` option. Unfortunately, the resulting calibration solutions yielded unrealistically large and highly scattered D-term values, indicating that the polarization calibration was unreliable. As a consequence, we were unable to derive meaningful polarization measurements from the earlier dataset.

2.5.2. Radio Spectral Analysis

Dense sampling of the radio spectrum starts at $T_0 + 17$ days, right after the rapid decay of the optical and X-ray afterglows. In this phase, the optical emission begins to be dominated by the SN light, whereas the X-rays show an afterglow rebrightening.

As shown in Figure 6, at low frequencies ($\lesssim$4 GHz), the radio flux shows a steep rise, characteristic of an optically thick spectrum. At higher frequencies, the spectral shape is instead consistent with optically thin emission. We model the radio spectral energy distribution (SED) using a smoothly broken power law based on a synchrotron spectrum. The function consists of three power-law segments with slopes of -2, $-1/3$, and $(p-1)/2$, separated by two spectral breaks corresponding to the self-absorption frequency ν_a and the characteristic synchrotron frequency ν_m, with $\nu_m > \nu_a$. A smoothness parameter s controls the sharpness of the transitions between the different segments.

We simultaneously fit the data from six epochs ($T_0 + 17$, 25, 36, 50, 55 and 62 days), allowing ν_a, ν_m, and the normalization to vary between epochs. We adopted log-uniform priors for ν_a and ν_m, and a uniform prior on the electron power-law index p over the range [2, 3]. The parameter p was assumed to be common to all epochs, while the smoothness parameter was fixed. For the two adjacent epochs of 50 and 55 days, we additionally imposed a common value of ν_a and ν_m to better constrain the fit using their complementary spectral coverage. The likelihood incorporates a 5% systematic calibration error added in quadrature to the statistical flux uncertainties.

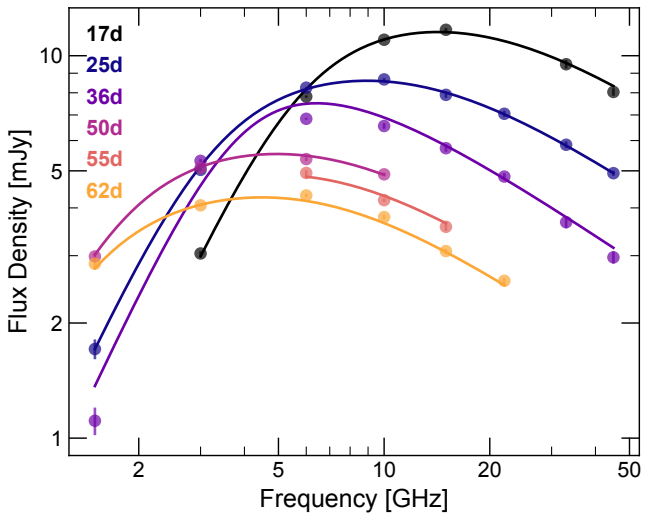


Figure 6. Radio SEDs of GRB 260310A at five epochs ($T_0 + 17$, 25, 36, 50, 55 and 62 days, color coded from dark to light). Solid curves are the best-fit SEDs assuming a smoothness parameter $s = 2$.

The radio SED and best-fit models for $s = 2$ are shown in Figure 6. From the fit, we derive $2 \lesssim p \lesssim 2.3$, depending on the adopted smoothness parameter. The peak flux decays with time as $\propto t^{-0.7}$, whereas the characteristic frequencies decrease as $\nu_m \sim \nu_{m,0}\, t^{-1.42}$ and $\nu_a \sim \nu_{a,0}\, t^{-0.54}$, where $\nu_{m,0} \approx 17$ GHz and $\nu_{a,0} \approx 5$ GHz at 17 days. At $T_0 + 50$ days, the derived values of $\nu_m \approx 6$ GHz and $\nu_a \approx 2$ GHz deviate from this trend.

3. Discussion

3.1. GRB 260310A in Context

In Figure 7 (left), we compare the X-ray (top), optical (middle), and radio (bottom) afterglows of GRB 260310A with those of GRBs with known redshifts. Our comparison sample includes 485 X-ray light curves from the Swift-XRT Database (P. A. Evans et al. 2009), 467 optical light curves from the repository of M. G. Dainotti et al. (2024),[25] and 64 events from the radio samples of S. Dichiara et al. (2022) and A. Gulati et al. (2026).[26]

To construct the X-ray light curves, we retrieve the count-rate data and the corresponding spectral information (unabsorbed counts-to-flux ratio and photon index) from the Swift online repository.[27] The unabsorbed flux light curves are derived by applying the corresponding time-averaged counts-to-flux conversion factors, then transformed into rest-frame luminosity light curves by accounting for cosmological time dilation and applying the appropriate k-correction (e.g., J. S. Bloom et al. 2001; V. Mangano et al. 2006).

To derive the optical light curves, we use the compilation of 535 GRBs with optical afterglow data (M. G. Dainotti et al. 2024, corrected for Galactic extinction), and filter for valid

[25] https://github.com/SLAC-Gamma-Rays/grbLC
[26] https://github.com/ashnagulati/Transient_Comparison_Plots
[27] https://www.swift.ac.uk/xrt_products

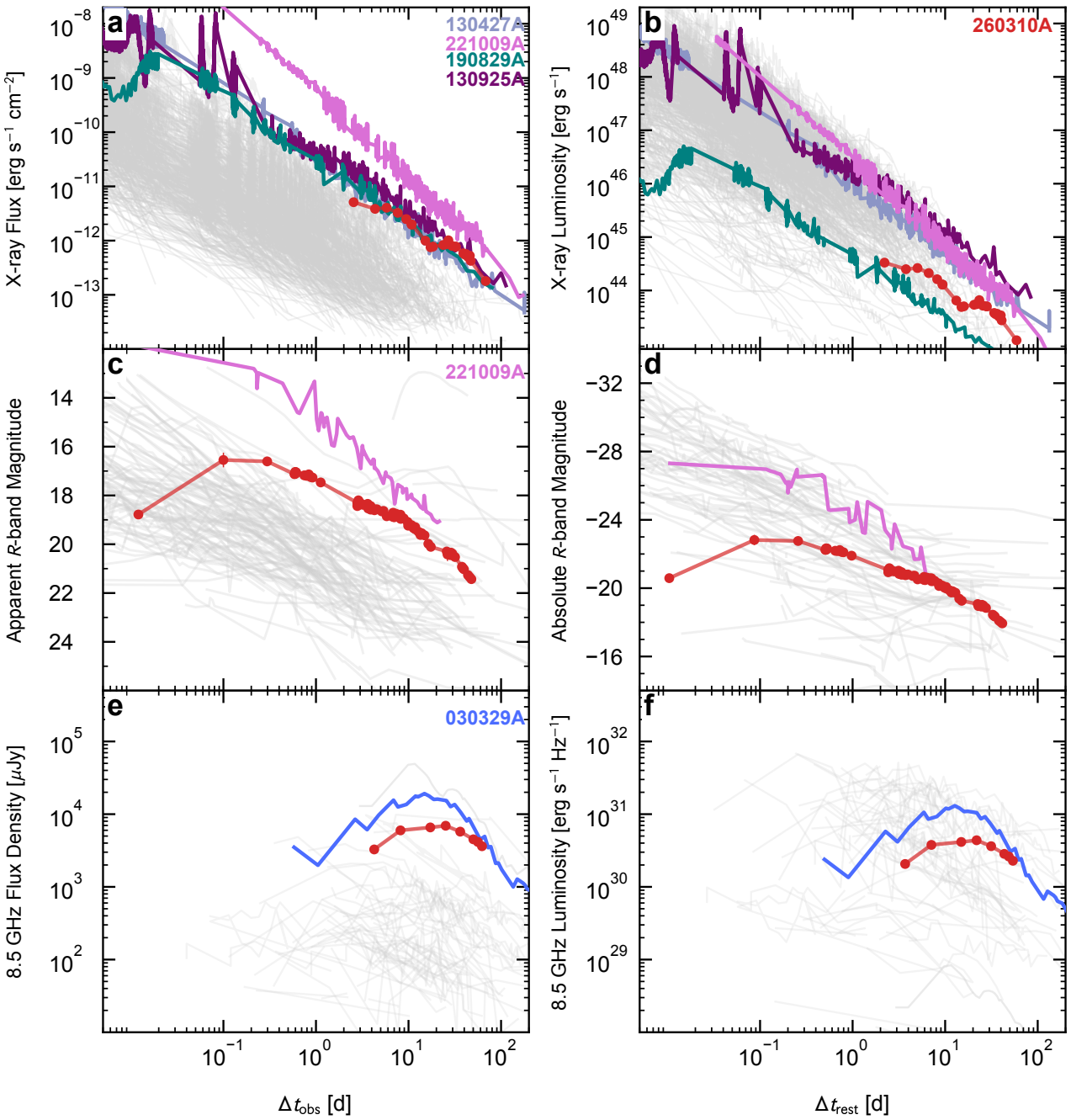


Figure 7. Comparison of GRB 260310A with the broader population of GRB afterglows with known redshifts. The panels display the observer-frame X-ray flux (0.3–10 keV; top left), rest-frame X-ray luminosity (0.3–10 keV; top right), optical apparent magnitude (R band; middle left), optical absolute magnitude (R band; middle right), radio observed flux density (8.5 GHz; bottom left) and radio rest-frame luminosity (8.5 GHz; bottom right).

photometric measurements near the R band. This selection yields a subsample of 467 light curves in the observer's frame, as displayed in Figure 7(c). To derive the rest-frame R-band light curves (Figure 7(d)), the observed magnitudes from different filters are shifted to the rest-frame R band and converted into absolute magnitudes. This step accounts for distance modulus correction, k-correction (e.g., D. A. Kann et al. 2010, which incorporates a redshift-dependent term and a spectral-index-dependent color term), and cosmological time dilation. In cases where the spectral index is not tabulated, the color correction is omitted only for observed wavelengths sufficiently close to the rest-frame R band. This yields a sample of 368 standardized light curves. A similar approach is adopted to build the rest-frame radio light curves (e.g., P. Chandra & D. A. Frail 2012; S. Dichiara et al. 2022).

In the observer's frame, GRB 260310A stands out at all wavelengths as one of the brightest afterglows ever detected: its X-ray flux lies in the top 1% of the distribution, its optical emission peaks at $\sim$16.5 AB mag at $\sim$0.2 day and then surpasses in brightness 99% of the sample, whereas its radio counterpart also tops the distribution of observed fluxes (brighter than 95% of the sample). However, this extreme apparent brightness is largely driven by its proximity. At a redshift of $z \approx 0.153$, GRB 260310A lies within the closest $\sim$3% of the GRB population, which significantly boosts its observed flux across all bands.

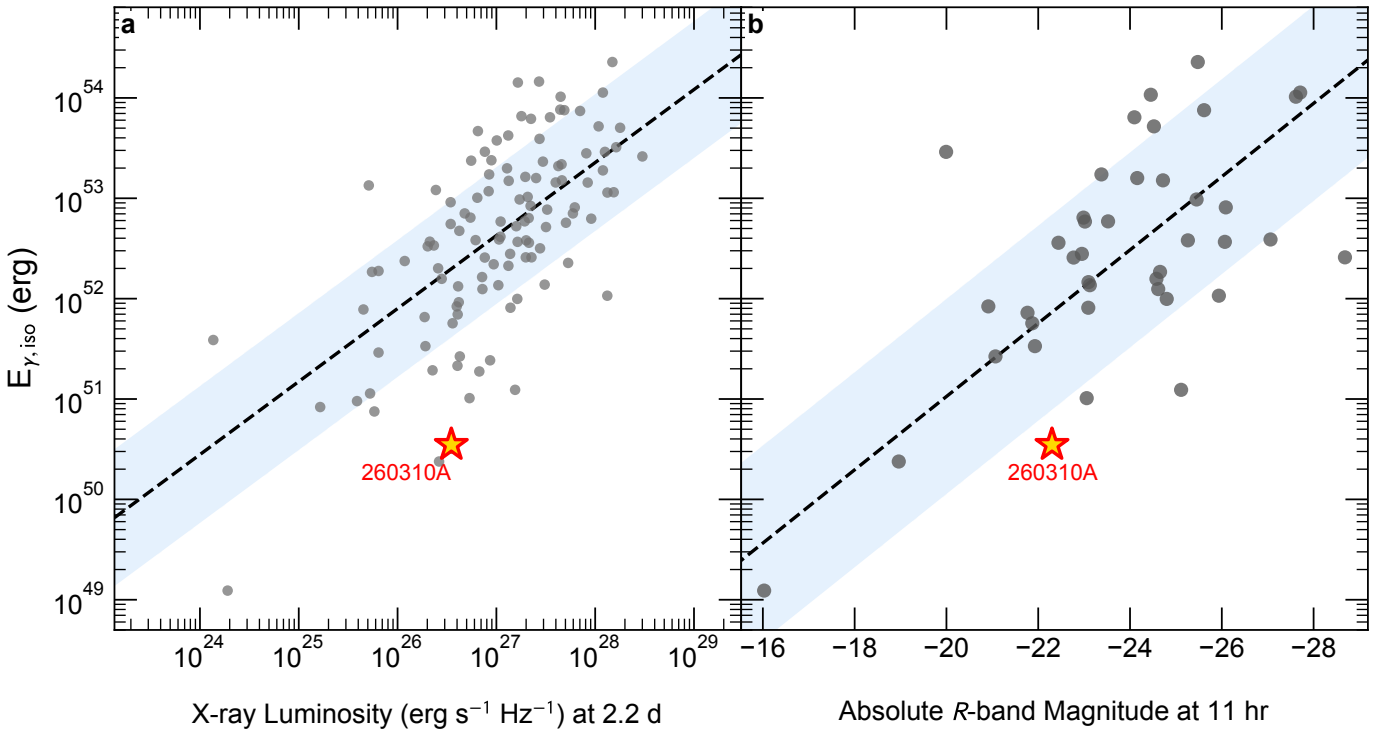


Figure 8. Afterglow rest-frame X-ray luminosity at rest-frame 2.2 days (a) and R-band absolute magnitude M_R at rest-frame 11 hr (b) vs. 10–1000 keV prompt emission isotropic-equivalent energy for a sample of GRBs detected by Fermi/GBM. The red-edged star highlights GRB 260310A. Black dashed lines and shaded area represent the best-fit log-linear correlations and the corresponding 1σ bands.

In the rest-frame (Figure 7, right column), GRB 260310A falls instead well within the broad distribution of cosmological GRBs. Its X-ray, optical, and radio luminosities cluster around the median values of the population, within a factor of a few of the typical afterglow luminosities, indicating no extreme properties once distance effects are removed. Both its time-averaged and peak radio luminosities are consistent with the median of the population. Its peak optical magnitude is fainter than roughly 80% of the sample, while its X-ray luminosity lies in the lower 15% of the distribution. It is only at later times, following its X-ray rebrightening, that its X-ray luminosity approaches extreme events such as GRB 221009A (M. A. Williams et al. 2023; B. O'Connor et al. 2023) and GRB 130427A (A. Maselli et al. 2014).

Nevertheless, its apparent brightness is not its only peculiar feature. GRB afterglow brightness shows a broad correlation with the prompt gamma-ray energy output (E. Berger 2007; P. D'Avanzo et al. 2012), reflecting the common origin in the relativistic flow. GRB 260310A instead exhibits a relatively modest gamma-ray fluence of $5.2^{+0.6}_{-0.3} \times 10^{-6}$ erg cm^{-2}, placing it at 66% of GBM GRBs, yet displays with one of the brightest optical, radio and X-ray afterglows. As shown in Figure 8, this clearly separates it from the bulk of the GRB population, and is reminiscent of the behavior of GRB 150101B, a short GRB likely seen off-axis (E. Troja et al. 2018b). In this Figure we consider a sample of 112 GRBs jointly detected by Swift and Fermi, which are characterized by a broadband prompt emission spectrum to infer $E_{\gamma,\mathrm{iso}}$ along with afterglow measurements to probe the blastwave kinetic energy. Optical luminosities were evaluated at a common time of 11 hr rest frame, whereas X-ray luminosities were calculated at a rest-frame frequency of 1 keV and at a common rest-frame time of 2.2 days to match our coverage of GRB 260310A. To bring GRB 260310A into agreement with the prompt afterglow correlations, the burst would require an isotropic-equivalent gamma-ray energy of $\gtrsim 10^{52}$ erg, nearly 2 orders of magnitude larger than the observed value. Observational biases affect the discovery of low-luminosity bursts (low $E_{\gamma,\mathrm{iso}}$) with faint afterglows (low L_X and L_{opt}), but they cannot explain why the right part of the diagram, corresponding to bright afterglows, remains sparsely populated. This suggests that GRB 260310A occupies an unusual region of the parameter space, where standard on-axis GRBs are rarely found.

Moreover, as shown in Figure 1(c), the GRB prompt emission properties deviate from the locus of long GRBs in the Amati plane (L. Amati et al. 2002; L. Amati 2006). Its low isotropic-equivalent energy—near the bottom of the observed distribution—combined with a standard peak energy places it close to the region typically occupied by short GRBs, initially complicating its classification. However, the spectroscopic identification of an associated SN unambiguously establishes a massive-star progenitor. We therefore interpret its inconsistency with the Amati relation as a viewing angle effect, where a modest offset θ_v from the jet axis reduces the Doppler boosting, significantly lowering the prompt γ-ray output ($E_{\gamma,\mathrm{iso}} \propto \theta_v^{-6}$) while only mildly shifting the spectral peak to lower energies ($E_{\mathrm{p}} \propto \theta_v^{-2}$; J. Granot et al. 2002).

Several GRBs have been classified as candidate off-axis events on the basis of their low isotropic-equivalent energies and spectral properties. GRB 980425, one of the closest GRBs ever detected ($z = 0.0085$), was associated with SN 1998bw and found to be less luminous by several orders of magnitude compared to the cosmological GRB population (E. Pian et al. 2000; L. Amati 2006; B. Zhang et al. 2009). R. Yamazaki et al. (2003) suggested that its soft spectrum and low E_{iso} could be reconciled with a standard long GRB viewed at a large angle

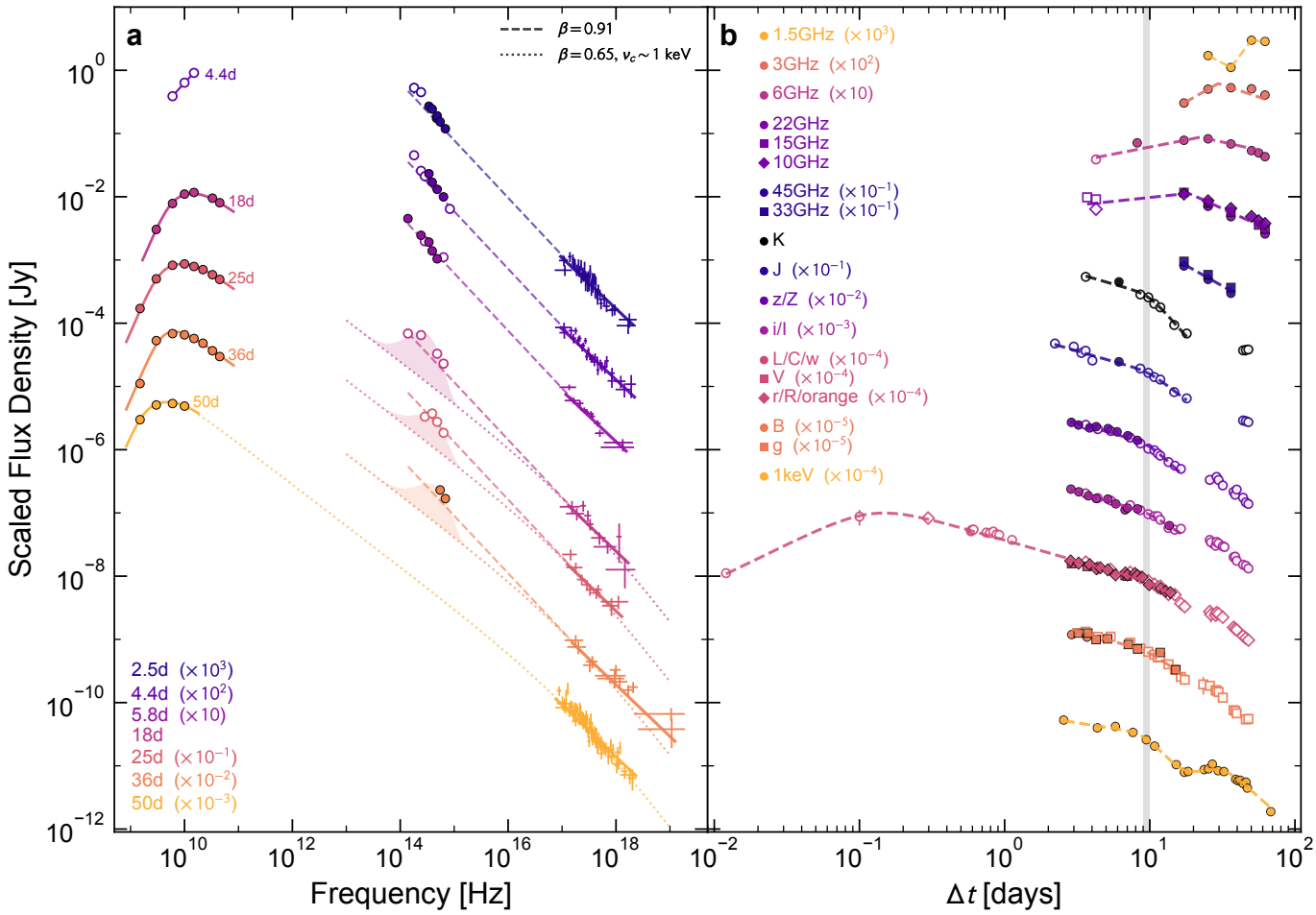


Figure 9. Multiwavelength observations of GRB 260310A. Filled markers are data obtained in this work, with complementary public data shown as open markers. Data are rescaled for display. a. SED from 2.5 days to 50 days. The dashed lines show the extrapolation from 1 keV to the K band assuming a power-law spectrum with $\beta = 0.91$. This model can bridge the optical/NIR and X-ray bands at all epochs. However, such an extrapolation would leave little room for the SN emission that instead dominates the optical bands. The dotted lines indicate a smoothly broken synchrotron model with $\beta \sim 0.65$ and $\nu_c \sim 1$ keV, which allows for an additional SN component (shaded blackbody models). (b). Multiwavelength light curves ranging from X-ray (bottom), through optical and NIR, to radio frequencies (top). The vertical band marks the observed temporal break in the X-ray and optical/NIR data.

from the jet axis. A similar suggestion was proposed for GRB 031203 (E. Ramirez-Ruiz et al. 2005; M. V. Ulanov et al. 2005; B. Zhang et al. 2009), another low-redshift ($z = 0.11$), SN-associated burst whose prompt emission properties place it as an outlier of the Amati relation. GRB 061021 and GRB 161219B, while less extreme in their energetics, also show spectral and energetic properties broadly consistent with mildly off-axis viewing geometries (L. Nava et al. 2012; Z. Cano et al. 2017). In addition, GRB 171205A ($z = 0.037$) was identified as a structured or two-component jet system, where the low prompt energy output and the late-time afterglow evolution were interpreted as the signature of a jet core observed at a modest offset (V. D'Elia et al. 2018; L. Izzo et al. 2019). These candidate off-axis events define an empirical locus in the $E_{\rm p}$–$E_{\rm iso}$ plane that is systematically offset from the standard Amati relation (F. Xu et al. 2023).

An off-axis jet for GRB 260310A naturally explains why the prompt γ-ray and early afterglow emission are suppressed while a comparatively bright afterglow is visible at later times, when the jet core has come into view. A viewing angle $(\theta_v - \theta_c) \approx$2–3 θ_c, where θ_c is the half-opening angle of the jet core, would be sufficient to reconcile the observed prompt emission properties with the Amati relation, while keeping the inferred energetics within the range of the long GRB population ($\approx 10^{52}$–10^{53} erg). A value as high as $(\theta_v - \theta_c) \approx 6\ \theta_c$ would instead push the total isotropic-equivalent gamma-ray energy above 10^{55} erg, comparable if not higher than GRB 221009A (S. Lesage et al. 2023; B. O'Connor et al. 2023).

3.2. Basic Afterglow Constraints

3.2.1. Evidence for a Bright Reverse Shock

The early X-ray and optical afterglows, from $T_0 + 2$ days to $T_0 + 14$ days, exhibit a similar (although not consistent within the errors) temporal behavior characterized by a shallow decay with slope ≈0.4–0.6, a temporal break at ∼9 days, and a steep decay $\alpha \approx 2$ (see Figure 4 and Figure 9(b)). Their spectral slopes, $\beta_X = 0.80 \pm 0.05$ and $\beta_o = 0.91^{+0.06}_{-0.09}$, are consistent with each other, and their flux densities align on the same power-law segment, with no evidence for a spectral break between the two bands (see Figure 9(a)).

Taken together, these results support the interpretation that the early optical and X-ray emission arises from the same spectral component and belongs to the same synchrotron segment. In the context of the standard synchrotron afterglow model (R. Sari et al. 1998; R. A. M. J. Wijers & T. J. Galama 1999), where the

observed radiation arises from a population of shock-accelerated electrons following a power-law energy distribution with index p, the optical-to-X-ray spectrum would be consistent either with the regime between the synchrotron characteristic frequency ν_m and the cooling frequency ν_c ($\nu_m < \nu_o < \nu_X < \nu_c$) for $p \approx 2.8$ or with the regime $\nu_m < \nu_c < \nu_o < \nu_X$ for $p \approx 1.8$.

Neither of these values of p is consistent with the flatter electron index, $p \approx 2$–2.3, inferred from the radio spectrum (Figure 6), which already suggests the presence of an additional emission component peaking at lower frequencies. We therefore consider a standard two-component scenario, as also discussed in C. T. Christy et al. (2026), in which the high-energy emission traces synchrotron radiation from the forward shock (FS) propagating into the external medium, while the low-energy spectrum is dominated by emission from a reverse shock (RS) traveling back into the ejecta (P. Mészáros & M. J. Rees 1997; R. Sari et al. 1999; S. Kobayashi 2000; B. Zhang et al. 2003; A. Gomboc et al. 2008).

Our initial hypothesis is that, throughout the entire temporal evolution, the nonthermal optical and X-ray emission belong to the same power-law segment of the FS component. However, this interpretation breaks down at late times. As the X-ray emission undergoes a rebrightening without any significant spectral evolution (Section 2.2), extrapolating the X-ray spectrum into the optical band would overpredict the observed optical flux, as illustrated in Figures 4 and 9(a). Furthermore, optical spectroscopy (see inset of Figure 4) provides clear evidence for the emergence of a SN component (B. O'Connor et al. 2026a) rather than a nonthermal power-law spectrum. Based on this evidence, we infer that a spectral break between the X-ray and optical bands must be present in order to reconcile all the observations. This implies that FS radiation is not the dominant component at optical and NIR wavelengths, as initially postulated. Instead, the observed emission is likely composed of a combination of FS+RS radiation at early times, gradually transitioning to a mixture of FS+SN emission at later epochs. An RS contribution helps explain the different X-ray and optical temporal slopes and the achromatic break at ∼9 days, which we interpret as a jet break. The RS polarized light would be diluted by the FS component, making this scenario consistent with the optical polarization limits (Section 2.3.2).

Given the complex afterglow evolution caused by the interplay of multiple components, standard closure relations for uniform or structured jets (e.g., H. Gao et al. 2013; G. Ryan et al. 2020) cannot be successfully applied, and it becomes challenging to map the transition from an RS-dominated to FS-dominated emission. Our polarimetric measurement helps in this respect. At $T_0 + 55$ days our radio observations probe the optically thin spectrum and derive a low degree of linear polarization (≈1.7%), consistent with typical FS values (J. Greiner et al. 2003; S. Covino & D. Gotz 2016; N. Mandarakas et al. 2023) and lower than the ≈3.2% polarization fraction derived by C. T. Christy et al. (2026) for the optically thin RS-dominated spectrum. Therefore, we conclude that at this epoch, FS radiation is the dominant nonthermal component, from radio to X-rays. The radio-to-X-ray spectral index is $\beta_{RX} \approx 0.65$, which implies an electron spectral index of $p \approx 2.3$. To explain the observed X-ray flux and spectral index $\beta_X \approx 0.8$, we estimate that the cooling frequency ν_c falls within the X-ray band, where its intrinsically smooth break prevents any sharp spectral transition within the X-ray band (see Figure 9(a)).

3.2.2. A Jet Viewed Off-axis

The early optical afterglow of GRB 260310A is characterized by an initial rising phase, brightening from ≈18.8 mag at 17 minutes to ≈16.7 mag at 0.3 day, before transitioning to a shallow decay with $\alpha_O \approx 0.6$. For highly relativistic outflows with Lorentz factors $\Gamma \gg 100$ viewed on-axis, the afterglow peak is expected to occur within minutes of the burst (E. Molinari et al. 2007), and is therefore rarely captured by follow-up observations (A. Panaitescu & W. T. Vestrand 2008; E. S. Rykoff et al. 2009; A. Melandri et al. 2014; M. G. Dainotti et al. 2024). A delayed peak may instead indicate either a moderately relativistic outflow, implying a relatively low initial Lorentz factor (e.g., V. M. Lipunov et al. 2022; A. Y. Q. Ho et al. 2022), or a geometric effect, such as an observer viewing angle offset from the jet axis (e.g., C. Guidorzi et al. 2009; T. Krühler et al. 2009; E. Troja et al. 2017, 2018b).

Adopting a luminosity of $L \sim 10^{49}$ erg s^{-1} and a variability timescale of $\Delta t_{\rm min} \lesssim 5$ s, a Lorentz factor of $\Gamma \gtrsim 10$ would be sufficient to explain the observed gamma-ray spectrum. This value is consistent with a moderately baryon-loaded ("dirty") fireball (B. Paczyński 1998; C. D. Dermer et al. 1999), indicating that compactness arguments alone cannot discriminate between low-Lorentz factor outflows and geometric effects in this event.

Polarization does not provide a decisive diagnostic either. Significant linear polarization is expected from geometric asymmetry, such as an off-axis viewing configuration (E. M. Rossi et al. 2004; G. Birenbaum et al. 2026). However, the degree of polarization and its temporal evolution depend sensitively on the jet structure, magnetic field geometry, RS contribution, and spectral regime. In the case of GRB 260310A, the combination of FS and RS components, along with limited temporal sampling of the polarimetric measurements and the depolarization by synchrotron self-absorption at low radio frequencies (T. W. Jones & S. L. O'Dell 1977), prevents a unique interpretation.

Additional insights come from the Amati diagram: the burst exhibits a peak energy that is harder than the average population of long GRBs with similar energetics. Baryon-loaded outflows are instead expected to produce softer spectra, as the reduced Lorentz factor lowers the characteristic photon energies (B. Zhang & P. Mészáros 2002b; T. Sakamoto et al. 2005). The relatively hard spectrum of GRB 260310A tends to disfavor a dirty fireball, whereas it remains consistent with a classical GRB seen off-axis (see also Section 3.1).

The temporal slope of the afterglow light curve will be shaped by (pre-)deceleration dynamics, jet geometry, or a combination of both. An optical FS light curve observed between ν_m and ν_c (as argued in Section 3.2.1) will have an asymptotic rising slope t^3 prior to deceleration. This holds for both jets observed fully on-axis and off-axis, assuming the line of sight is included within the beaming cone of flow coasting at constant Lorentz factor $\Gamma(\theta)$, i.e., $\theta_v - \theta_{\rm w} < 1/\Gamma(\theta_{\rm w})$. An off-axis observer, however, would see a more extended period of turnover across the peak, leading to an apparently shallower rise in case the full asymptotic rise stage is not captured by observation.

An observer far off-axis, with $\theta_v - \theta_{\rm w} > 1/\Gamma(\theta_{\rm w})$, will see an even steeper rise following $t^{(15-3p)/2} \sim t^{4.1}$ (assuming

$p \sim 2.3$), once the jet has begun to decelerate, regardless of jet structure. After the jet truncation angle θ_w has entered into the field of view, a rising temporal slope of $\alpha < 0$ is still possible for a smoothly structured jet (e.g., a Gaussian or power-law jet, rather than a two-component jet), if the observer angle θ_v is sufficiently larger than the core angle θ_c (G. Ryan et al. 2020).

However, if the jet is viewed off-axis, but the observer angle θ_ν follows $\theta_c < \theta_\nu < \theta_w$, the temporal slope due to jet structure will not be negative but instead lead to a shallower decline than predicted by an on-axis model (top hat or structured). In this interpretation, the prepeak light curve for GRB 260310A can be attributed to predeceleration coasting, whereas the relatively shallow postpeak slope (compared to top-hat models) reflects emission from higher energy angles of the flow closer to the jet axis gradually entering the line of sight. The turnover at 9 days is then a consequence of the outer truncation angle of the jet coming into view, i.e., when $1/\Gamma(\theta_w) \sim \theta_w - \theta_\nu$. The presence of a late-time rebrightening is consistent with the hypothesis that GRB 260310A is seen off-axis, as we will discuss below.

3.2.3. Origin of the Late-time Afterglow Rebrightening

Long-lasting X-ray emission has been observed in other nearby GRBs (C. Kouveliotou et al. 2004; R. Margutti et al. 2013), typically with spectra softer than those of standard afterglows and therefore often interpreted as arising from an additional emission component. In GRB 260310A, inverse-Compton (IC) scattering of SN optical photons (R. A. Chevalier & C. Fransson 2006) would be an intriguing possibility, since the X-ray bump occurs on a timescale comparable to the expected SN peak (B. O'Connor et al. 2026a). In such a scenario, if the seed blackbody photons are scattered by the bulk of the shocked electrons, with $\gamma_e \sim \gamma_m$, the characteristic upscattered frequency would be $\nu_{\rm BB,IC} \sim \gamma_m^2 \nu_{\rm BB}$, where γ_m is the minimum Lorentz factor of the accelerated electrons. This can be recast as

$$\nu_{\rm BB,IC} \sim 1.9 \times 10^{19} \left(\frac{\epsilon_B}{10^{-3}}\right)^{-\frac{1}{2}} \left(\frac{\Gamma}{10}\right)^{-2} \times \left(\frac{\nu_m}{10^{10}\rm Hz}\right) \left(\frac{\nu_{\rm BB}}{10^{15}\rm Hz}\right) \left(\frac{n_{\rm ext}}{1\rm cm^{-3}}\right)^{-\frac{1}{2}} \rm Hz. \quad (2)$$

Thus, for typical parameters, the IC peak is expected to lie at or above the X-ray band, rather than producing a featureless X-ray component with little spectral evolution. This, together with the observed luminosity, $L_X \approx 10^{43}\,\rm erg\,s^{-1}$, disfavors an IC origin of the X-ray emission. Instead, the stable X-ray spectral index and the radio SED indicate that synchrotron emission from the FS remains the dominant component in the X-ray band.

As shown in Figure 10, afterglow rebrightenings on rest-frame timescales of ~1–10 days are sporadically observed in GRBs and fast X-ray transients (FXTs) and are commonly interpreted as episodes of late energy injection refreshing the blast wave (M. J. Rees & P. Mészáros 1998). In this context, GRB 260310A shows a rebrightening that evolves on somewhat longer timescales, ~20–30 days, and is fainter than most events in the comparison sample. However, the observed diversity of late-time afterglows is poorly characterized and strongly affected by selection biases. In the optical band, the SN onset would mask most of these late-time brightenings. More in general, follow-up observations are typically

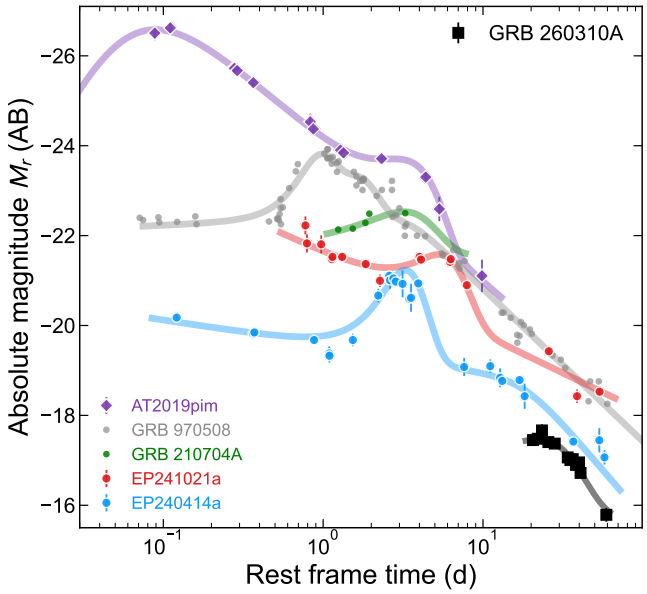


Figure 10. The rebrightening of GRB 260310A (black squares), scaled from X-rays to optical assuming $\nu_c \approx$ 0.1 keV and a power-law index of $\beta \sim 0.6$. A sample of late-time afterglow rebrightenings, including AT2019pim (D. A. Perley et al. 2025), GRB 970508 (T. J. Galama et al. 1998b), GRB 210704A (assuming $z \approx 2.3$; R. L. Becerra et al. 2023), EP241021a (M. Busmann et al. 2025), and EP240414a (H. Sun et al. 2025), is shown for comparison.

interrupted once the afterglow becomes faint, and only events considered especially interesting, such as GRB 260310A, are monitored with sufficient cadence and depth to reveal their late-time structures. For instance, a query of the full Swift X-ray afterglow archive (P. A. Evans et al. 2009) shows that only ~1% of the sample, 13 out of more than 1300 long GRBs, have X-ray coverage extending beyond 15 days. An inspection of the optical catalog of M. G. Dainotti et al. (2024) returns similar results. The apparent rarity of late-time afterglow rebrightenings may therefore reflect, at least in part, the limited temporal and spectral coverage of most monitoring campaigns rather than their intrinsic absence.

In the case of GRB 260310A, its off-axis geometry may offer an alternative route to explain the late-time X-ray rebrightening. A gradual afterglow rebrightening can be expected when a structured (or two-component) jet is viewed off-axis (e.g., P. Beniamini et al. 2022). In this framework, the early optical afterglow is dominated by the wider and less energetic component, which exhibits a jet break at ~9 days as the nearest outer jet edge comes into view (i.e., $1/\Gamma(\theta_w) \sim \theta_w - \theta_\nu$). For an off-axis observer viewing a two-component jet, this might well occur before the inner component enters the line of sight. The later X-ray bump is then attributed to this narrower and more energetic jet core, which becomes visible only after sufficient deceleration reduces relativistic beaming and brings its emission into the observer's line of sight. Thus, the two afterglow peaks, at ~0.1 day and ~25 days, could be interpreted as the emergence of distinct angular components of the outflow.

A two-component jet structure has often been invoked to explain the evolution of the brightest GRBs and their afterglows, whose behavior deviates from canonical closure relations. A remarkable example is the recent GRB 221009A, for which the extreme brightness of the prompt emission and the absence of a jet break in the afterglow data would imply an energy crisis unless a complex jet structure is taken into

account (B. O'Connor et al. 2023; Y. Sato et al. 2025). A similar geometry has also been proposed to explain the origin of some gamma-ray dark fast X-ray transients characterized by late-time rebrightening (M. Busmann et al. 2025; M. Yadav et al. 2025; G. Gianfagna et al. 2025; H. Sun et al. 2025; J.-H. Zheng et al. 2025). In the case of GRB 260310A, a narrow gamma-ray-emitting core surrounded by broader and less energetic wings and seen off-axis could account for the peculiar X-ray afterglow evolution, the delayed afterglow onset and the burst location in the Amati plane.

3.3. Afterglow Modeling

We fit the broadband data using `VegasAfterglow` (Y. Wang et al. 2026), which allows us to include both FS and RS components. The modeling is based on the standard external shock synchrotron emission from a relativistic jet interacting with the circumburst medium (P. Mészáros & M. J. Rees 1997; R. Sari et al. 1998; R. A. M. J. Wijers & T. J. Galama 1999; J. Granot & R. Sari 2002; J. Granot et al. 2002; H. van Eerten & A. MacFadyen 2013; G. Ryan et al. 2020).

The intrinsic energetics and dynamics are governed by the isotropic-equivalent kinetic energy $E_{k,\rm iso}$ and the initial Lorentz factor Γ_0, while the microphysical properties are described by the fractions of shock energy partitioned into electrons ϵ_e and magnetic fields ϵ_B, along with the power-law index of the electron energy distribution p. The jet profile is characterized by the core half-opening angle θ_c, supplemented by the energy distribution index k_e and the Lorentz factor distribution index k_g for the power-law structured model. The observer's viewing angle $\theta_{\rm v}$ is treated as a free parameter to account for off-axis effects. In all cases, the fraction of accelerated electrons is fixed at $\xi_e = 1$. We tested different jet geometries, including uniform, Gaussian, and power-law profiles, as well as a two-component jet. The parameter space was explored using the Python package `pymultinest` (J. Buchner et al. 2014).

We find that a simple FS model from an off-axis structured jet provides a reasonable description of the broadband light curves, from radio to X-rays (Figure A1 left panel). By using a flat spectral index $p \approx 2$ (Figure A1 right panel) and a uniform density ($n_{\rm ISM}$) environment, the model can reproduce most of our dataset up to $\sim$ 20 days, when the X-ray afterglow brightens. This model has $\nu_a \approx 6$ GHz, $\nu_m \approx 12$ GHz, and $\nu_c \approx 3 \times 10^{14}$ Hz at 17 days. However, this solution is driven by our limited coverage of the hard X-ray and millimeter range, which are systematically underpredicted by the FS model, the similar behavior of the X-ray and optical/NIR light curves (Section 3.2.1), and it does not account for the SN contribution in the optical range. Therefore, whereas this model roughly describes the observed light curves and spectra, it does not fully reproduce the physics of the explosion.

No combination of RS + FS provides a better fit for either a uniform or a wind-like density profile. This is not unexpected, as the empirical description of the radio SEDs (Section 2.5.2) already revealed that the spectral evolution deviates from standard predictions, and suggests that a more complex scenario is required, potentially involving mechanisms such as energy injection and refreshed shocks. These could also be used to explain the late-time bump of the X-ray light curve.

As discussed in Section 3.2.3, we also test whether the late-time emission could be interpreted as the emergence of a second narrow jet seen off-axis. We model the X-ray data and the radio data after $T_0 + 50$ days with a simple FS model from a two-component jet expanding into a uniform medium. This model (Figure A2) can reproduce the late-time bump with a narrow, highly relativistic and energetic jet core, with $\theta_c \approx 0.8^\circ$, $\Gamma \approx 150$, and $E_{\rm K,iso} \approx 2 \times 10^{54}$ erg, viewed at an angle of $\theta_v \approx 10^\circ$. The core is surrounded by a broader, slower, and less energetic jet component, with $\theta_w \approx 16^\circ$, $\Gamma \approx 15$, and $E_{\rm K,iso} \approx 5 \times 10^{52}$ erg, which accounts for the early X-ray emission.

4. Summary

We presented multiwavelength observations of the nearby ($z \sim 0.153$) GRB 260310A and its extremely bright and long-lived afterglow, placing it among the top $\sim$1% of the GRB afterglow population. The burst is characterized by a modest gamma-ray energy release paired with a relatively hard peak energy, which classifies it as an outlier of the Amati relation. We showed that viewing effects solve the apparent tension in the burst's properties. The slow rise and delayed onset of its optical afterglow support the scenario of a jet seen off-axis.

Our analysis of the broadband spectrum favors the presence of two emission components: a bright RS dominating the radio and extending to the optical band, and an FS contributing to the optical and dominating in the X-rays. In support of this picture, we infer a decreased degree of linear polarization, from $\Pi \sim 3.2\%$ to $\sim$ 1.7%, mapping the transition from RS- to FS-dominated emission. However, as often occurs for bright GRB afterglows, none of our standard RS plus FS models, testing different jet structures and density profiles, can successfully reproduce the full broadband dataset and its temporal evolution, suggesting a departure from the simplest afterglow prescriptions.

Our long-term X-ray monitoring of the X-ray afterglow identifies a peculiar late-time rebrightening at $\sim$20–30 days, after a phase of rapid decay. This behavior is difficult to accommodate within a single FS model and may instead indicate a late episode of energy injection that refreshes the shock or additional structure in the outflow, such as a two-component jet. A low-velocity jet seen (approximately) on-axis would not be able to combine the early peak and late rebrightening in a single jet model, whereas an off-axis two-component jet can accommodate both these peaks.

Acknowledgments

This work is supported by the European Research Council through the Consolidator grant BHianca (grant agreement ID 101002761).

A.J.C.T. acknowledges support from the Spanish Ministry project No. PID2023-151905OB-I00 and Junta de Andalucía grant No. P20_010168. A.J.C.T. expresses his sincere thanks to the staff of the San Pedro Mártir Observatory in México and IHSM/UMA-CSIC La Mayora in Spain for their assistance in the operation of the 0.6 m Javier Gorosabel and TELMA telescopes at the BOOTES-5 and BOOTES-2 stations, respectively.

Data were partially collected with the 0.9 m and 1.5 m telescopes at the OSN operated by the Instituto de Astrofísica de Andalucía (IAA-CSIC), and based on observations collected at the Centro Astronómico Hispano en Andalucía (CAHA) at Calar Alto (proposal 26A-2.2-026), operated jointly by Junta de Andalucía and Consejo Superior de Investigaciones Científicas (IAA-CSIC).

This work is based on the data obtained with EP, a space mission supported by the Strategic Priority Program on Space

Science of the Chinese Academy of Sciences, in collaboration with the European Space Agency, the Max-Planck-Institute for extraterrestrial Physics (Germany), and the Centre National d'Études Spatiales (France).

We acknowledge the support from the LBT-Italian Coordination Facility for the execution of observations, data distribution, and reduction. Reduction and analysis by the LBT Imaging Data Center at INAF-OARoma. The LBT is an international collaboration among institutions in Italy, the United States, and Germany. LBT Corporation Members are: Istituto Nazionale di Astrofisica, Italy; The University of Arizona on behalf of the Arizona Board of Regents; LBT Beteiligungsgesellschaft, Germany, representing the Max-Planck Society, The Leibniz Institute for Astrophysics Potsdam, and Heidelberg University; The Ohio State University, representing OSU, University of Notre Dame, University of Minnesota, and University of Virginia. Observations have benefited from the use of ALTA Center (alta.arcetri.inaf.it) forecasts performed with the Astro-Meso-Nh model. Initialization data of the ALTA automatic forecast system come from the General Circulation Model (HRES) of the European Centre for Medium Range Weather Forecasts.

This research has made use of data obtained from the Chandra Data Archive provided by the Chandra X-ray Center (CXC). This Letter employs a list of Chandra datasets, obtained by the Chandra X-ray Observatory, contained in doi:10.25574/cdc.620.

Sky-background data are provided by `ATRAN` (S. D. Lord 1992) and the Gemini Observatory.

Software: `astropy` (Astropy Collaboration et al. 2013, 2018, 2022), `Matplotlib` (J. D. Hunter 2007), `SciPy` (P. Virtanen et al. 2020), `NumPy` (C. R. Harris et al. 2020), `pandas` (Wes McKinney 2010), `Source Extractor` (E. Bertin & S. Arnouts 1996), `SFFT` (L. Hu et al. 2022), `SAOImageDS 9` (W. A. Joye & E. Mandel 2003), `dustmaps` (G. Green 2018), `dust_extinction` (K. D. Gordon 2024), `VegasAfterglow` (Y. Wang et al. 2026), `HEASoft` (NASA High Energy Astrophysics Science Archive Research Center (HEASARC) 2014).

Appendix
Details of Optical Observations

BOOTES. Two robotic telescopes, BOOTES-2 (Spain) and BOOTES-5 (México) were used, and observations were carried out in the Sloan g', r', i', and UKIRT Z filters, covering from $T_0 + 3$ days to $T_0 + 15$ days, with seeing of $\sim 1.8''$–$4.6''$. We employed the saccadic fast Fourier transform (SFFT) algorithm (L. Hu et al. 2022) to isolate the transient emission from the host galaxy background.

OSN. Observations were conducted using the 1.5 m telescope (T150) and the 0.9 m telescope (T90) in the Johnson–Cousins filters B, V, R, I (2×2 binning) starting from $\sim T_0 + 3$ days. The average seeing was $1.5''$ for T150 and $2.5''$ for T90. Image reduction and photometry were performed using `MaxIm DL` v6.13. Photometric calibration was performed using Pan-STARRS DR1 (K. C. Chambers et al. 2016) reference stars, converted to the *BVRI* system with the Lupton (2005)[28] color-transformation equations.

Ondřejov. Observations at the Ondřejov Observatory (Czech Republic) were conducted using three telescopes. The 2×20 cm Small Binocular Telescope (SBT; J. Štrobl et al. 2019) was employed with the Sloan g', r', and i' filters. Concurrent high-cadence monitoring in the Sloan r' band (8 epochs between $T_0 + 4$ days and $T_0 + 14$ days) were provided by the 0.5 m robotic telescope (D50; J. Štrobl et al. 2023). The 2.0 m Perek telescope (O2m) contributed to the campaign, utilizing the Sloan g' filter at the beginning of the observations ($T_0 + 4$ days). The typical seeing was $\sim 3''$ throughout the observations at Ondřejov. Image processing consisted of per-frame dark and flat-field calibration, followed by inverse-variance-weighted coaddition via the `pyrt` pipeline (M. Jelínek 2023); SBT frames were additionally drizzled prior to coaddition owing to the undersampled plate scale of that instrument. Host-galaxy contamination was removed by subtraction of a Pan-STARRS DR1 template using `hotpants` (A. Becker 2015).

LBT. We used the LBT Utility Camera in the Infrared (LUCI), with J and K filters, and the Large Binocular Camera (LBC), with r and z filters, instruments mounted on LBT under program ID IT-2025B-047 (PI: Troja). LUCI observed at $T_0 + 6.1$ days with an average air mass of 1.4 and seeing of $0.''7$. LBC observed at $T_0 + 8.2$ days with an average air mass of 1.3 and mean seeing of $1.''1$. We subtracted the host contamination for r and z filters against archival Legacy Survey images using the SFFT.

The observed magnitudes, uncorrected for Galactic extinction, are listed in Table A1.

XMM-Newton OM. The XMM-Newton OM conducted simultaneous observations using the *U*, *V*, *B*, *UVW1*, *UVW2*, and *UVM2* filters while EPIC was acquiring X-ray data. The exposure times were 8.8 ks for the *UVW2* filter and 4.4 ks for the remaining filters. Data were processed using SAS `omichain`. Whereas optical images are dominated by the galaxy's light, in the ultraviolet filters a faint source is detected at the GRB position with $m_{UVW2} = 21.7 \pm 0.4$ AB mag (corrected for extinction along the sight line). However, based on a single epoch, we cannot assess whether the source is transient or associated with an underlying star-forming knot (B. O'Connor et al. 2026a).

The broadband light curves with the afterglow modeling (Section 3.3) are shown in Figures A1 and A2.

[28] https://www.sdss4.org/dr12/algorithms/sdssubvritransform/#Lupton2005.

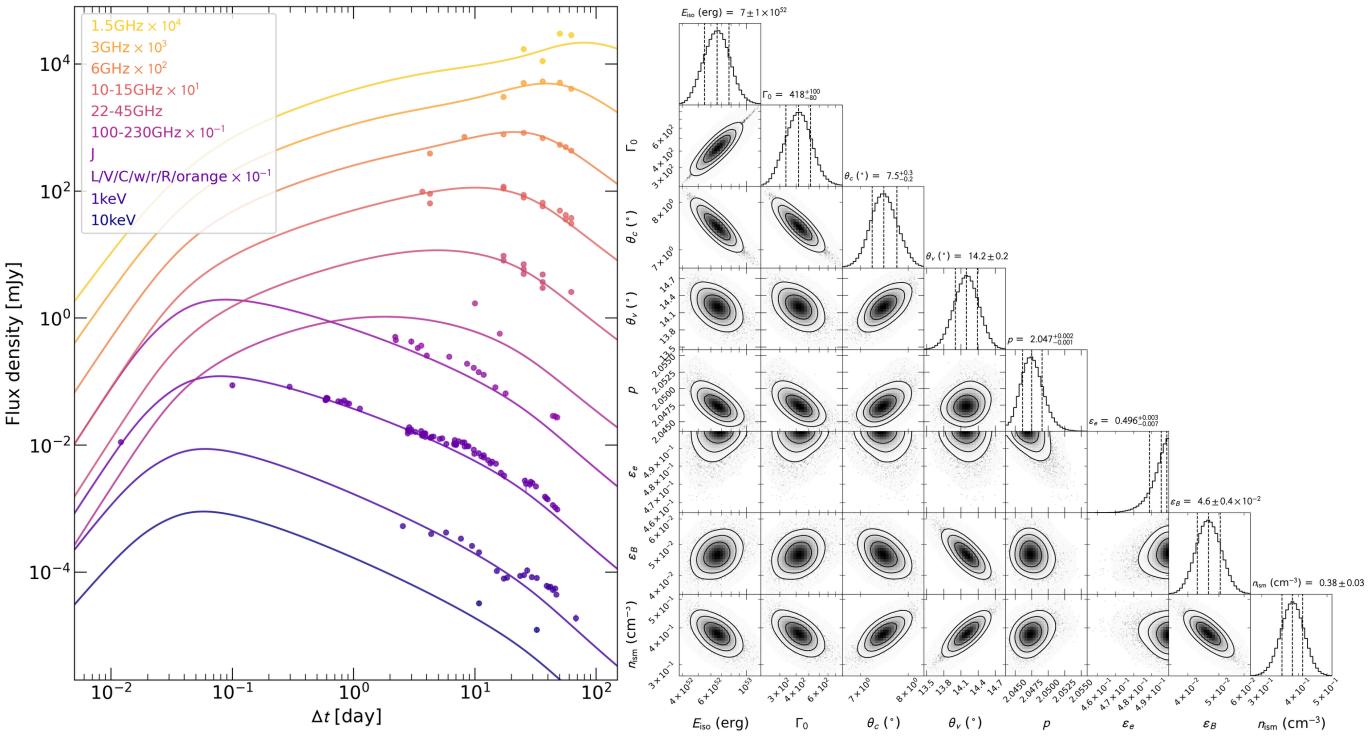


Figure A1. Left: multiwavelength light curves of GRB 260310A together with the best-fit Gaussian jet FS model in an interstellar medium (ISM) environment. Right: posterior distributions of the model parameters. The median values and corresponding 1σ uncertainties are indicated above the one-dimensional marginalized histograms.

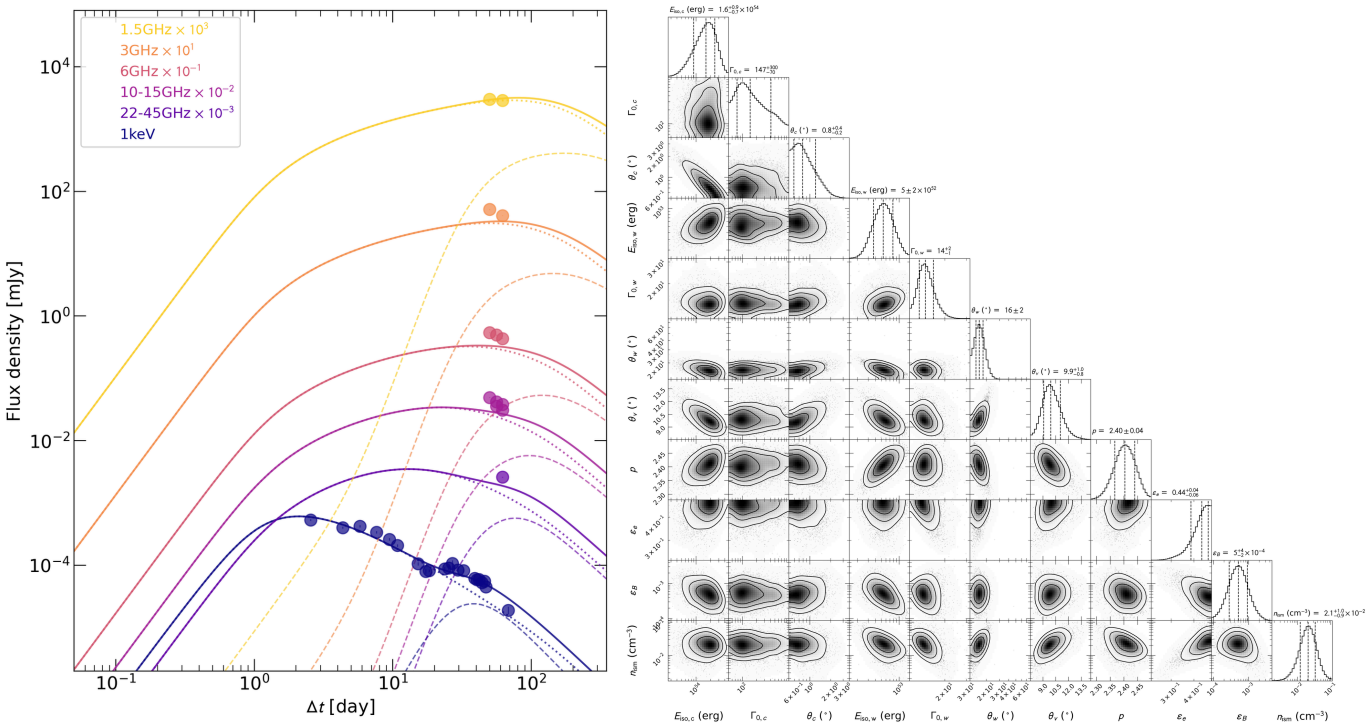


Figure A2. Left: multiwavelength light curves of GRB 260310A together with the best-fit FS emission from the two-component jet in an ISM environment, adopted to describe the X-ray and late radio data. In this scenario, the early optical and radio emission are dominated by an RS and are treated as upper limits in the fit. Right: posterior distributions of the model parameters. The median values and corresponding 1σ uncertainties are indicated above the one-dimensional marginalized histograms.

Table A1
Log of X-Ray, Optical, NIR, and Radio Observations of GRB 260310A

X-Ray Date (UT)	Δt (days)	Telescope	Exposure (ks)	Flux (erg cm^{-2} s^{-1})	Flux Density (mJy)
2026-03-12 18:12:41	2.55	EP/FXT-A+B	3.3	$5.1 \pm 0.2 \times 10^{-12}$	$5.3 \pm 0.2 \times 10^{-4}$
2026-03-14 13:23:51	4.35	EP/FXT-A+B	3.9	$3.9 \pm 0.1 \times 10^{-12}$	$4.0 \pm 0.1 \times 10^{-4}$
2026-03-16 00:01:31	5.79	EP/FXT-A+B	3.0	$4.0 \pm 0.1 \times 10^{-12}$	$4.2 \pm 0.2 \times 10^{-4}$
2026-03-17 20:44:25	7.66	EP/FXT-A+B	2.8	$3.3 \pm 0.1 \times 10^{-12}$	$3.4 \pm 0.1 \times 10^{-4}$
2026-03-19 15:51:50	9.45	EP/FXT-A+B	2.8	$2.5 \pm 0.1 \times 10^{-12}$	$2.6 \pm 0.1 \times 10^{-4}$
2026-03-21 00:01:09	10.8	NuSTAR/FPM-A+B	27.6	$2.8 \pm 0.1 \times 10^{-12}$ (3–79 keV)	$3.2 \pm 0.3 \times 10^{-5}$ (10 keV)
2026-03-21 06:11:59	11.1	EP/FXT-A+B	2.7	$1.98 \pm 0.07 \times 10^{-12}$	$2.1 \pm 0.1 \times 10^{-4}$
2026-03-25 10:00:09	15.2	EP/FXT-A+B	4.9	$10.0 \pm 0.5 \times 10^{-13}$	$1.05 \pm 0.06 \times 10^{-4}$
2026-03-27 12:19:52	17.3	EP/FXT-A+B	2.9	$7.5 \pm 0.6 \times 10^{-13}$	$7.9^{+0.7}_{-0.6} \times 10^{-5}$
2026-03-28 13:52:35	18.4	EP/FXT-A+B	9.0	$7.8 \pm 0.4 \times 10^{-13}$	$8.1 \pm 0.4 \times 10^{-5}$
2026-04-02 21:37:07	23.7	EP/FXT-A+B	3.3	$8.3 \pm 0.6 \times 10^{-13}$	$8.7^{+0.7}_{-0.6} \times 10^{-5}$
2026-04-04 13:32:46	25.4	EP/FXT-A+B	3.3	$8.5 \pm 0.6 \times 10^{-13}$	$9.0^{+0.7}_{-0.6} \times 10^{-5}$
2026-04-06 03:58:19	27.0	EP/FXT-A+B	1.0	$1.0 \pm 0.1 \times 10^{-12}$	$1.1 \pm 0.1 \times 10^{-4}$
2026-04-08 18:17:16	29.6	EP/FXT-A+B	2.6	$8.0^{+0.6}_{-0.7} \times 10^{-13}$	$8.4 \pm 0.7 \times 10^{-5}$
2026-04-11 15:12:08	32.4	EP/FXT-A+B	4.2	$7.7 \pm 0.4 \times 10^{-13}$	$8.1 \pm 0.5 \times 10^{-5}$
2026-04-11 16:53:39	32.5	NuSTAR/FPM-A+B	12.8	$1.07^{+0.08}_{-0.09} \times 10^{-12}$ (3–79 keV)	$1.2 \pm 0.1 \times 10^{-5}$ (10 keV)
2026-04-18 06:59:52	39.1	EP/FXT-A+B	2.7	$5.8^{+0.5}_{-0.6} \times 10^{-13}$	$6.1 \pm 0.6 \times 10^{-5}$
2026-04-19 18:54:26	40.6	EP/FXT-A+B	6.2	$5.5 \pm 0.3 \times 10^{-13}$	$5.8 \pm 0.3 \times 10^{-5}$
2026-04-20 02:43:29	40.9	Chandra/ACIS	5.0	…	…
2026-04-21 04:38:25	42.0	EP/FXT-A+B	3.2	$5.6 \pm 0.5 \times 10^{-13}$	$5.9 \pm 0.5 \times 10^{-5}$
2026-04-23 05:06:26	44.0	EP/FXT-A+B	2.9	$5.0 \pm 0.5 \times 10^{-13}$	$5.2 \pm 0.5 \times 10^{-5}$
2026-04-25 04:59:20	46.0	EP/FXT-A+B	3.0	$5.3 \pm 0.3 \times 10^{-13}$	$5.5 \pm 0.3 \times 10^{-5}$
2026-04-25 09:46:04	46.2	EP/FXT-A+B	9.2	…	…
2026-04-26 05:11:21	47.0	XMM/pn+MOS	∼20	$4.2 \pm 0.1 \times 10^{-13}$	$4.4 \pm 0.1 \times 10^{-5}$
2026-05-17 07:43:43	68.1	Chandra/ACIS	9.9	$1.8 \pm 0.2 \times 10^{-13}$	$1.9^{+0.3}_{-0.2} \times 10^{-5}$

Optical/NIR Date (UT)	Δt (days)	Telescope	Exposure (ks)	Filter	Magnitude (AB)
2026-03-13 00:02:18	2.80	T90	0.3	*R*	18.35 ± 0.02
2026-03-13 00:07:34	2.80	T90	0.3	*V*	18.49 ± 0.03
2026-03-13 00:45:52	2.83	T150	9.3	*R*	18.41 ± 0.01
2026-03-13 01:32:07	2.85	CAHA	0.03	*i*	17.97 ± 0.08
2026-03-13 01:56:45	2.87	BOOTES	0.9	*r*	18.25 ± 0.04
2026-03-13 02:04:11	2.88	BOOTES	1.0	*i*	18.02 ± 0.05
2026-03-13 02:11:39	2.89	BOOTES	1.0	*Z*	17.85 ± 0.05
2026-03-13 02:33:57	2.90	T90	0.9	*B*	18.79 ± 0.06
2026-03-13 04:33:57	2.98	T90	0.6	*R*	18.34 ± 0.03
2026-03-13 04:39:12	2.99	T90	0.6	*V*	18.43 ± 0.01
2026-03-13 10:04:20	3.21	BOOTES	3.3	*g*	18.72 ± 0.02
2026-03-13 10:27:04	3.23	BOOTES	3.5	*Z*	17.95 ± 0.04
2026-03-13 10:36:59	3.24	BOOTES	3.2	*r*	18.43 ± 0.02
2026-03-13 10:43:41	3.24	BOOTES	3.2	*i*	18.10 ± 0.03
2026-03-13 20:59:38	3.67	T90	1.5	*V*	18.59 ± 0.01
2026-03-13 21:17:43	3.68	T150	0.9	*R*	18.50 ± 0.01
2026-03-13 21:36:35	3.69	T90	2.4	*B*	18.89 ± 0.02
2026-03-13 22:02:17	3.71	SBT	29.2	*i*	18.27 ± 0.10
2026-03-13 22:34:40	3.73	T90	1.2	*V*	18.55 ± 0.02
2026-03-13 22:44:27	3.74	O2m	1.3	*g*	18.76 ± 0.03
2026-03-13 23:07:52	3.76	SBT	37.1	*g*	18.68 ± 0.05
2026-03-14 00:49:56	3.83	BOOTES	1.8	*r*	18.49 ± 0.06
2026-03-14 01:02:18	3.84	BOOTES	2.0	*i*	18.25 ± 0.09
2026-03-14 01:17:50	3.85	BOOTES	2.1	*Z*	18.07 ± 0.06
2026-03-14 02:23:36	3.89	D50	13.6	*r*	18.48 ± 0.02
2026-03-14 02:29:58	3.90	T150	2.7	*R*	18.63 ± 0.01
2026-03-14 11:22:37	4.27	BOOTES	1.5	*g*	18.98 ± 0.04
2026-03-14 11:23:50	4.27	BOOTES	0.7	*i*	18.36 ± 0.09
2026-03-14 11:30:51	4.27	BOOTES	0.7	*Z*	18.02 ± 0.08
2026-03-14 11:42:53	4.28	BOOTES	1.1	*r*	18.66 ± 0.04
2026-03-14 18:30:39	4.56	SBT	3.4	*r*	18.62 ± 0.10

Table A1
(Continued)

2026-03-15 07:54:14	5.12	BOOTES	1.3	*g*	18.95 ± 0.03
2026-03-15 08:08:44	5.13	BOOTES	1.5	*r*	18.70 ± 0.03
2026-03-15 08:15:30	5.14	BOOTES	1.5	*i*	18.39 ± 0.10
2026-03-15 08:39:12	5.15	BOOTES	1.4	*Z*	18.09 ± 0.06
2026-03-16 00:25:03	5.81	BOOTES	1.2	*r*	18.90 ± 0.07
2026-03-16 00:49:32	5.83	BOOTES	1.0	*i*	18.58 ± 0.09
2026-03-16 03:43:11	5.95	BOOTES	0.7	*Z*	18.22 ± 0.07
2026-03-16 08:07:33	6.13	LUCI	0.2	*J*	17.94 ± 0.01
2026-03-16 08:07:33	6.13	LUCI	0.2	*K*	17.27 ± 0.01
2026-03-16 22:59:36	6.75	T150	0.3	*I*	18.82 ± 0.01
2026-03-16 23:04:50	6.76	T150	0.3	*R*	18.88 ± 0.01
2026-03-16 23:10:05	6.76	T150	0.3	*V*	18.93 ± 0.01
2026-03-17 00:32:00	6.82	D50	2.1	*r*	18.76 ± 0.04
2026-03-17 04:14:15	6.97	T150	0.6	*I*	18.86 ± 0.03
2026-03-17 04:37:22	6.99	T150	0.6	*R*	18.91 ± 0.03
2026-03-17 04:47:41	6.99	T150	0.6	*V*	18.95 ± 0.01
2026-03-17 05:44:39	7.03	BOOTES	1.0	*r*	18.90 ± 0.03
2026-03-17 05:54:10	7.04	BOOTES	1.0	*i*	18.64 ± 0.04
2026-03-17 06:03:42	7.05	BOOTES	1.0	*Z*	18.38 ± 0.07
2026-03-17 07:45:04	7.12	BOOTES	0.7	*g*	19.17 ± 0.03
2026-03-18 02:40:38	7.91	D50	10.7	*r*	18.84 ± 0.04
2026-03-18 09:25:02	8.20	LBC	0.1	*z*	18.54 ± 0.05
2026-03-18 09:25:07	8.20	LBC	0.1	*r*	18.84 ± 0.08
2026-03-18 10:21:43	8.23	BOOTES	0.7	*r*	19.01 ± 0.03
2026-03-18 10:25:38	8.23	BOOTES	0.7	*i*	18.78 ± 0.04
2026-03-18 10:29:31	8.23	BOOTES	0.7	*Z*	18.58 ± 0.07
2026-03-18 10:29:52	8.23	BOOTES	1.0	*g*	19.35 ± 0.03
2026-03-19 02:06:51	8.88	D50	14.4	*r*	18.99 ± 0.04
2026-03-20 02:52:01	9.91	D50	8.7	*r*	19.29 ± 0.04
2026-03-22 00:12:28	11.80	SBT	27.3	*g*	19.49 ± 0.11
2026-03-22 02:02:18	11.88	D50	14.2	*r*	19.44 ± 0.03
2026-03-23 01:54:01	12.87	D50	14.8	*r*	19.55 ± 0.04
2026-03-23 20:16:56	13.64	BOOTES	0.9	*i*	19.44 ± 0.13
2026-03-24 01:46:40	13.87	D50	14.2	*r*	19.60 ± 0.04
2026-03-25 07:53:04	15.12	BOOTES	1.1	*g*	20.17 ± 0.08
Supplementary optical/NIR data from public resources					
	0.012	GOTO		*L*	18.84 ± 0.06[1]
	0.100	DDOTI		*w*	16.60 ± 0.30[2]
	0.297	ATLAS		Orange	16.65 ± 0.03[3]
	0.585	LAST		Clear	17.18 ± 0.04[4]
	0.590	LAST		Clear	17.17 ± 0.04[4]
	0.596	LAST		Clear	17.09 ± 0.04[4]
	0.600	LAST		Clear	17.16 ± 0.04[4]
	0.606	LAST		Clear	17.10 ± 0.04[4]
	0.611	LAST		Clear	17.11 ± 0.04[4]
	0.749	LAST		Clear	17.23 ± 0.04[4]
	0.792	LAST		Clear	17.25 ± 0.04[4]
	0.835	LAST		Clear	17.19 ± 0.04[4]
	0.879	LAST		Clear	17.30 ± 0.04[4]
	0.917	LAST		Clear	17.32 ± 0.04[4]
	1.12	DDOTI		*w*	17.52 ± 0.01[2]
	2.21	WINTER		*J*	17.16 ± 0.09[5]
	2.23	WINTER		*J*	17.28 ± 0.09[5]
	2.99	WINTER		*J*	17.34 ± 0.12[5]
	3.38	SYSU		*J*	17.59 ± 0.10[6]
	4.02	TNG		*J*	17.89 ± 0.10[7]

Radio Date (UT)	Δt (days)	Telescope	Exposure (ks)	Frequency (GHz)	Flux Density (mJy)
2026-03-13 23:20	3.7	AMI-LA	28.8	15.2 (Ku)	9.8 ± 0.5[8]
2026-03-14 10:22	4.26	VLA	0.898	6 (C)	3.9 ± 0.2[9]
2026-03-14 10:22	4.26	VLA	0.778	10 (X)	6.4 ± 0.3[9]
2026-03-14 10:22	4.26	VLA	0.539	15 (Ku)	9.1 ± 0.5[9]
2026-03-18 10:35	8.19	VLA	0.898	6 (C)	7.1 ± 0.4

Table A1
(Continued)

2026-03-20	10	NOEMA	...	100 (W)	17.0 ± 0.9^{10}
2026-03-26	16	SMA	...	230	5.7 ± 0.2^{11}
2026-03-27 10:20	17.2	VLA	0.359	3 (S)	3.04 ± 0.04
2026-03-27 10:20	17.2	VLA	0.479	6 (C)	7.82 ± 0.06
2026-03-27 10:20	17.2	VLA	0.479	10 (X)	11.01 ± 0.07
2026-03-27 10:20	17.2	VLA	0.598	15 (Ku)	11.69 ± 0.11
2026-03-27 10:20	17.2	VLA	1.197	33 (Ka)	9.50 ± 0.24
2026-03-27 10:20	17.2	VLA	1.795	45 (Q)	8.04 ± 0.18
2026-04-04 10:30	25.2	VLA	0.359	1.5 (L)	1.71 ± 0.10
2026-04-04 10:30	25.2	VLA	0.359	3 (S)	5.03 ± 0.04
2026-04-04 10:30	25.2	VLA	0.479	6 (C)	8.25 ± 0.04
2026-04-04 10:30	25.2	VLA	0.479	10 (X)	8.67 ± 0.07
2026-04-04 10:30	25.2	VLA	0.479	15 (Ku)	7.90 ± 0.14
2026-04-04 10:30	25.2	VLA	1.277	22 (K)	7.05 ± 0.13
2026-04-04 10:30	25.2	VLA	1.096	33 (Ka)	5.85 ± 0.12
2026-04-04 10:30	25.2	VLA	1.496	45 (Q)	4.93 ± 0.08
2026-04-15 05:30	36.0	VLA	0.363	1.5 (L)	1.11 ± 0.08
2026-04-15 05:30	36.0	VLA	0.359	3 (S)	5.31 ± 0.05
2026-04-15 05:30	36.0	VLA	0.479	6 (C)	6.84 ± 0.03
2026-04-15 05:30	36.0	VLA	0.479	10 (X)	6.55 ± 0.11
2026-04-15 05:30	36.0	VLA	0.455	15 (Ku)	5.73 ± 0.12
2026-04-15 05:30	36.0	VLA	1.117	22 (K)	4.83 ± 0.10
2026-04-15 05:30	36.0	VLA	0.987	33 (Ka)	3.67 ± 0.13
2026-04-15 05:30	36.0	VLA	1.316	45 (Q)	2.97 ± 0.10
2026-04-29 08:40	50.2	VLA	0.978	1.5 (L)	2.98 ± 0.05
2026-04-29 08:40	50.2	VLA	0.598	3 (S)	5.10 ± 0.07
2026-04-29 08:40	50.2	VLA	0.479	6 (C)	5.37 ± 0.06
2026-04-29 08:40	50.2	VLA	0.479	10 (X)	4.90 ± 0.05
2026-05-05 04:25	55.0	VLA	0.239	6 (C)	4.94 ± 0.07
2026-05-05 04:25	55.0	VLA	0.239	10 (X)	4.19 ± 0.03
2026-05-05 04:25	55.0	VLA	0.239	15 (Ku)	3.57 ± 0.09
2026-05-11 07:20	62.1	VLA	0.479	1.5 (L)	2.86 ± 0.07
2026-05-11 07:20	62.1	VLA	0.359	3 (S)	4.06 ± 0.03
2026-05-11 07:20	62.1	VLA	0.479	6 (C)	4.31 ± 0.05
2026-05-11 07:20	62.1	VLA	0.479	10 (X)	3.79 ± 0.05
2026-05-11 07:20	62.1	VLA	0.455	15 (Ku)	3.08 ± 0.04
2026-05-11 07:20	62.1	VLA	1.117	22 (K)	2.58 ± 0.04

Note. Δt represents the midtime of the observation relative to the trigger time T_0. An error of 0.3 mag was associated to the DDOTI measurement to account for uncertainties in the photometric calibration.

References. 1. D. O'Neill et al. 2026, 2. R. L. Becerra et al. 2026, 3. J. Tonry et al. 2026 (https://www.wis-tns.org/object/2026fgk), 4. R. Konno et al. 2026, 5. R. Stein et al. 2026, 6. J.-J. Li et al. 2026, 7. R. Brivio et al. 2026, 8. L. Rhodes et al. 2026, 9. S. Giarratana et al. 2026, 10. A. Ho et al. 2026a, 11. A. Ho et al. 2026b.

(This table is available in its entirety in machine-readable form in the online article.)

ORCID iDs

Yu-Han Yang https://orcid.org/0000-0003-0691-6688
Roberto Ricci https://orcid.org/0000-0003-4631-1528
Eleonora Troja https://orcid.org/0000-0002-1869-7817
Muskan Yadav https://orcid.org/0009-0004-9520-5822
Yi-Han Iris Yin https://orcid.org/0000-0002-5596-5059
Rubén Sánchez-Ramírez https://orcid.org/0000-0002-7158-5099
Brendan O'Connor https://orcid.org/0000-0002-9700-0036
Niccolò Passaleva https://orcid.org/0009-0007-6886-4082
Alberto J. Castro-Tirado https://orcid.org/0000-0003-2999-3563
Hendrik van Eerten https://orcid.org/0000-0002-8680-8718
Simone Dichiara https://orcid.org/0000-0001-6849-1270
Vincenzo Galluzzi https://orcid.org/0000-0003-1394-7044
Narjes Shahamat Dehsorkh https://orcid.org/0009-0009-7526-4522
Iván Agudo https://orcid.org/0000-0002-3777-6182
Jesús Aceituno https://orcid.org/0000-0003-0487-1105
Malte Busmann https://orcid.org/0009-0001-0574-2332
Maria D. Caballero-García https://orcid.org/0000-0001-7920-4564
Emilio Fernández-García https://orcid.org/0009-0009-4604-9639
Daniel Gruen https://orcid.org/0000-0003-3270-7644
Maria Gritsevich https://orcid.org/0000-0003-4268-6277
Sergiy Guziy https://orcid.org/0000-0003-2628-6468
David Hiriart https://orcid.org/0000-0002-4711-7658
You-Dong Hu https://orcid.org/0000-0002-7400-4608
Martin Jelínek https://orcid.org/0000-0003-3922-7416
Alexander Kutyrev https://orcid.org/0000-0002-2715-8460
Alzbeta Malenakova https://orcid.org/0000-0002-0636-9138
Filip Novotny https://orcid.org/0009-0008-5788-3584

Ignacio Pérez-García https://orcid.org/0000-0002-7273-3671
Shashi B. Pandey https://orcid.org/0000-0002-1474-1980
Jorma Ryske https://orcid.org/0009-0009-4453-8260
Alfredo Sota https://orcid.org/0000-0002-9404-6952
Jan Strobl https://orcid.org/0000-0002-4147-2878
Hira Waseem https://orcid.org/0009-0001-2089-9899
Siyu Wu https://orcid.org/0009-0004-7113-8258

References

Abbott, B. P., Abbott, R., Abbott, T. D., et al. 2017, PhRvL, 119, 161101,
Amati, L. 2006, MNRAS, 372, 233
Amati, L., Frontera, F., Tavani, M., et al. 2002, A&A, 390, 81
Arnaud, K. A. 1996, ASPC, 101, 17
Astropy Collaboration, Price-Whelan, A. M., Lim, P. L., et al. 2022, ApJ, 935, 167
Astropy Collaboration, Price-Whelan, A. M., Sipőcz, B. M., et al. 2018, AJ, 156, 123
Astropy Collaboration, Robitaille, T. P., Tollerud, E. J., et al. 2013, A&A, 558, A33
Atteia, J.-L., Moreno Méndez, E., Lincetto, M., et al. 2026, GCN Circular, 43981, 1
Balasubramanian, A., Corsi, A., Mooley, K. P., et al. 2022, ApJ, 938, 12
Becerra, R. L., Troja, E., Watson, A. M., et al. 2023, MNRAS, 522, 5204
Becerra, R. L., Watson, A. M., Angulo Valdez, C., et al. 2026, GCN, 43991, 1
Becker, A. 2015, HOTPANTS: High Order Transform of PSF ANd Template Subtraction, Astrophysics Source Code Library., ascl:1504.004
Beniamini, P., Gill, R., & Granot, J. 2022, MNRAS, 515, 555
Berger, E. 2007, ApJ, 670, 1254
Bertin, E., & Arnouts, S. 1996, A&AS, 117, 393
Birenbaum, G., Granot, J., & Beniamini, P. 2026, A&A, 706, A145
Bloom, J. S., Frail, D. A., & Sari, R. 2001, AJ, 121, 2879
Bloom, J. S., Kulkarni, S. R., & Djorgovski, S. G. 2002, AJ, 123, 1111
Brivio, R., Malesani, D., Izzo, L., et al. 2026, GCN, 44004, 1
Buchner, J., Georgakakis, A., Nandra, K., et al. 2014, A&A, 564, A125
Busmann, M., O'Connor, B., Sommer, J., et al. 2025, A&A, 701, A225
Cano, Z., Izzo, L., de Ugarte Postigo, A., et al. 2017, A&A, 605, A107
CASA Team, Bean, B., Bhatnagar, S., et al. 2022, PASP, 134, 114501
Castro-Tirado, A. J. 2023, NatAs, 7, 1136
Chakyar, S. P., & Resmi, L. 2025, ApJ, 983, 111
Chambers, K. C., Magnier, E. A., Metcalfe, N., et al. 2016, arXiv:1612.05560
Chandra, P., & Frail, D. A. 2012, ApJ, 746, 156
Chevalier, R. A., & Fransson, C. 2006, ApJ, 651, 381
Christy, C. T., Laskar, T., Alexander, K. D., et al. 2026, ApJL, 1006, L8
Costa, E., Frontera, F., Heise, J., et al. 1997, Natur, 387, 783
Covino, S., & Gotz, D. 2016, A&AT, 29, 205
Dainotti, M. G., De Simone, B., Mohideen Malik, R. F., et al. 2024, MNRAS, 533, 4023
D'Avanzo, P., Salvaterra, R., Sbarufatti, B., et al. 2012, MNRAS, 425, 506
de Ugarte Postigo, A., Geier, S., Izzo, L., et al. 2026, GCN, 44124, 1
Decleir, M., Gordon, K. D., Andrews, J. E., et al. 2022, ApJ, 930, 15
Delchambre, L., Bailer-Jones, C. A. L., Bellas-Velidis, I., et al. 2023, A&A, 674, A31
D'Elia, V., Campana, S., D'Aì, A., et al. 2018, A&A, 619, A66
Dermer, C. D., Chiang, J., & Böttcher, M. 1999, ApJ, 513, 656
Dey, A., Schlegel, D. J., Lang, D., et al. 2019, AJ, 157, 168
Dichiara, S., Troja, E., Lipunov, V., et al. 2022, MNRAS, 512, 2337
Escudero Pedrosa, J., Agudo, I., Morcuende, D., et al. 2024, AJ, 168, 84
Evans, P. A., Beardmore, A. P., Page, K. L., et al. 2009, MNRAS, 397, 1177
Fermi GBM Team 2026, GCN, 43951, 1
Fitzpatrick, E. L., Massa, D., Gordon, K. D., Bohlin, R., & Clayton, G. C. 2019, ApJ, 886, 108
Fong, W.-F., Nugent, A. E., Dong, Y., et al. 2022, ApJ, 940, 56
Frail, D. A., Kulkarni, S. R., Nicastro, L., Feroci, M., & Taylor, G. B. 1997, Natur, 389, 261
Fruscione, A., McDowell, J. C., Allen, G. E., et al. 2006, SPIE, 6270, 62701V
Gaia Collaboration, Vallenari, A., Brown, A. G. A., et al. 2023, A&A, 674, A1
Galama, T. J., Vreeswijk, P. M., van Paradijs, J., et al. 1998a, Natur, 395, 670
Galama, T. J., Groot, P. J., van Paradijs, J., et al. 1998b, ApJL, 497, L13
Gao, H., Lei, W.-H., Zou, Y.-C., Wu, X.-F., & Zhang, B. 2013, NewAR, 57, 141
Gehrels, N., & Mészáros, P. 2012, Sci, 337, 932
Gehrels, N., Norris, J. P., Barthelmy, S. D., et al. 2006, Natur, 444, 1044
Gianfagna, G., Piro, L., Bruni, G., et al. 2025, A&A, 703, A92
Giarratana, S., Giroletti, M., Ghirlanda, G., et al. 2026, GCN, 44045, 1
Goldstein, A., Veres, P., Burns, E., et al. 2017, ApJL, 848, L14
Golkhou, V. Z., & Butler, N. R. 2014, ApJ, 787, 90
Golkhou, V. Z., Butler, N. R., & Littlejohns, O. M. 2015, ApJ, 811, 93
Gomboc, A., Kobayashi, S., Guidorzi, C., et al. 2008, ApJ, 687, 443
Gordon, K. D. 2024, JOSS, 9, 7023
Gordon, K. D., Cartledge, S., & Clayton, G. C. 2009, ApJ, 705, 1320
Gordon, K. D., Clayton, G. C., Decleir, M., et al. 2023, ApJ, 950, 86
Gordon, K. D., Misselt, K. A., Bouwman, J., et al. 2021, ApJ, 916, 33
Gottlieb, O., & Nakar, E. 2022, MNRAS, 517, 1640
Gottlieb, O., Nakar, E., & Bromberg, O. 2021, MNRAS, 500, 3511
Granot, J., Panaitescu, A., Kumar, P., & Woosley, S. E. 2002, ApJL, 570, L61
Granot, J., & Sari, R. 2002, ApJ, 568, 820
Green, G. 2018, JOSS, 3, 695
Greiner, J., Klose, S., Reinsch, K., et al. 2003, Natur, 426, 157
Guetta, D., & Della Valle, M. 2007, ApJL, 657, L73
Guidorzi, C., Clemens, C., Kobayashi, S., et al. 2009, A&A, 499, 439
Gulati, A., Murphy, T., Kaplan, D. L., et al. 2026, ApJ, 1000, 118
Hallinan, G., Corsi, A., Mooley, K. P., et al. 2017, Sci, 358, 1579
Harris, C. R., Millman, K. J., van der Walt, S. J., et al. 2020, Natur, 585, 357
Harrison, F. A., Craig, W. W., Christensen, F. E., et al. 2013, ApJ, 770, 103
Ho, A., Bremer, M., & Schroeder, G. 2026a, GCN, 44057, 1
Ho, A., Keating, G., Alexander, K., Laskar, T., & Margutti, R. 2026b, GCN, 44134, 1
Ho, A. Y. Q., Perley, D. A., Yao, Y., et al. 2022, ApJ, 938, 85
Hu, L., Wang, L., Chen, X., & Yang, J. 2022, ApJ, 936, 157
Hu, Y.-D., Fernández-García, E., Caballero-García, M. D., et al. 2023, FrASS, 10, 952887
Huang, Y. F., Dai, Z. G., & Lu, T. 2002, MNRAS, 332, 735
Hunter, J. D. 2007, CSE, 9, 90
Izzo, L., de Ugarte Postigo, A., Maeda, K., et al. 2019, Natur, 565, 324
Jayaraman, R., Ho, A. Y. Q., Hinds, K.-R., et al. 2026, GCN, 43994, 1
Jelínek, M. 2023, CoSka, 53, 127
Jones, T. W., & O'Dell, S. L. 1977, ApJ, 214, 522
Joye, W. A., & Mandel, E. 2003, ASPC, 295, 489
Kammoun, E., Waratkar, G., Jayaraman, R., Hinds, K.-R., & Ho, A. Y. Q. 2026, GCN, 44063, 1
Kann, D. A., Klose, S., Zhang, B., et al. 2010, ApJ, 720, 1513
Kathirgamaraju, A., Barniol Duran, R., & Giannios, D. 2018, MNRAS, 473, L121
Kobayashi, S. 2000, ApJ, 545, 807
Konno, R., Garrappa, S., Zimmerman, E. A., et al. 2026, GCN, 43974, 1
Kouveliotou, C., Woosley, S. E., Patel, S. K., et al. 2004, ApJ, 608, 872
Krühler, T., Greiner, J., Afonso, P., et al. 2009, A&A, 508, 593
Lamb, G. P., Lyman, J. D., Levan, A. J., et al. 2019, ApJL, 870, L15
Lampton, M., Margon, B., & Bowyer, S. 1976, ApJ, 208, 177
Lazzati, D., Deich, A., Morsony, B. J., & Workman, J. C. 2017, MNRAS, 471, 1652
Lazzati, D., Perna, R., Morsony, B. J., et al. 2018, PhRvL, 120, 241103
Lesage, S., Veres, P., Briggs, M. S., et al. 2023, ApJL, 952, L42
Li, J.-J., Chen, C., Cao, D.-L., et al. 2026, GCN, 43993, 1
Liang, E., Zhang, B., Virgili, F., & Dai, Z. G. 2007, ApJ, 662, 1111
Lipunov, V. M., Kornilov, V. G., Topolev, V. V., et al. 2022, AstL, 48, 623
Lord, S. D. 1992, NASA Technical Memorandum 103957, https://ui.adsabs.harvard.edu/abs/1992nstc.rept.....L
Magnier, E. A., Chambers, K. C., Flewelling, H. A., et al. 2020, ApJS, 251, 3
Mandarakas, N., Blinov, D., Aguilera-Dena, D. R., et al. 2023, A&A, 670, A144
Mangano, V., La Parola, V., Troja, E., et al. 2006, NCimB, 121, 1297
Margutti, R., Soderberg, A. M., Wieringa, M. H., et al. 2013, ApJ, 778, 18
Margutti, R., Alexander, K. D., Xie, X., et al. 2018, ApJL, 856, L18
Maselli, A., Melandri, A., Nava, L., et al. 2014, Sci, 343, 48
McKinney, W. 2010, in Proc. of the 9th Python in Science Conf., ed. S. van der Walt & J. Millman, 56, doi:10.25080/Majora-92bf1922-00a
Meegan, C., Lichti, G., Bhat, P. N., et al. 2009, ApJ, 702, 791
Melandri, A., Virgili, F. J., Guidorzi, C., et al. 2014, A&A, 572, A55
Mészáros, P., & Rees, M. J. 1997, ApJ, 476, 232
Modjaz, M., Liu, Y. Q., Bianco, F. B., & Graur, O. 2016, ApJ, 832, 108
Molinari, E., Vergani, S. D., Malesani, D., et al. 2007, A&A, 469, L13
Mooley, K. P., Frail, D. A., Dobie, D., et al. 2018, ApJL, 868, L11
Nagakura, H., Hotokezaka, K., Sekiguchi, Y., Shibata, M., & Ioka, K. 2014, ApJL, 784, L28
Nakar, E., & Piran, T. 2017, ApJ, 834, 28
Narayan, R., Paczynski, B., & Piran, T. 1992, ApJL, 395, L83

NASA High Energy Astrophysics Science Archive Research Center (HEASARC) 2014, HEAsoft: Unified Release of FTOOLS and XANADU, Astrophysics Source Code Library,, ascl:1408.004
Nava, L., Salvaterra, R., Ghirlanda, G., et al. 2012, MNRAS, 421, 1256
O'Connor, B., Busmann, M., Hall, X. J., et al. 2026a, ApJ, 1006, 210
O'Connor, B., Toshikage, S., Tanaka, M., et al. 2026b, GCN, 44137, 1
O'Connor, B., Troja, E., Dichiara, S., et al. 2022, MNRAS, 515, 4890
O'Connor, B., Troja, E., Ryan, G., et al. 2023, SciA, 9, eadi1405
O'Neill, D., Ramsay, G., Ackley, K., et al. 2026, TNSTR, 2026-1001, 1
Paczyński, B. 1998, ApJL, 494, L45
Panaitescu, A., & Vestrand, W. T. 2008, MNRAS, 387, 497
Peng, F., Königl, A., & Granot, J. 2005, ApJ, 626, 966
Perley, D. A., Schroeder, G., & Laskar, T. 2026, GCN, 44160, 1
Perley, D. A., Ho, A. Y. Q., Fausnaugh, M., et al. 2025, MNRAS, 537, 2362
Perley, R. A., & Butler, B. J. 2017, ApJS, 230, 7
Pian, E., Amati, L., Antonelli, L. A., et al. 2000, ApJ, 536, 778
Piran, T. 2004, RvMP, 76, 1143
Planck Collaboration, Aghanim, N., Akrami, Y., et al. 2020, A&A, 641, A6
Pursiainen, M., Malesani, D. B., Leloudas, G., et al. 2026, GCN, 43990, 1
Racusin, J. L., Karpov, S. V., Sokolowski, M., et al. 2008, Natur, 455, 183
Ramirez-Ruiz, E., Celotti, A., & Rees, M. J. 2002, MNRAS, 337, 1349
Ramirez-Ruiz, E., Granot, J., Kouveliotou, C., et al. 2005, ApJL, 625, L91
Rastinejad, J. C., Gompertz, B. P., Levan, A. J., et al. 2022, Natur, 612, 223
Rees, M. J., & Mészáros, P. 1998, ApJL, 496, L1
Rhoads, J. E. 1999, ApJ, 525, 737
Rhodes, L., Hughes, A., Fender, R., et al. 2026, GCN, 44005, 1
Rossi, E., Lazzati, D., & Rees, M. J. 2002, MNRAS, 332, 945
Rossi, E. M., Lazzati, D., Salmonson, J. D., & Ghisellini, G. 2004, MNRAS, 354, 86
Ryan, G., van Eerten, H., MacFadyen, A., & Zhang, B.-B. 2015, ApJ, 799, 3
Ryan, G., van Eerten, H., Piro, L., & Troja, E. 2020, ApJ, 896, 166
Ryan, G., van Eerten, H., Troja, E., et al. 2024, ApJ, 975, 131
Rykoff, E. S., Aharonian, F., Akerlof, C. W., et al. 2009, ApJ, 702, 489
Sakamoto, T., Lamb, D. Q., Kawai, N., et al. 2005, ApJ, 629, 311
Sari, R., Piran, T., & Halpern, J. P. 1999, ApJL, 519, L17
Sari, R., Piran, T., & Narayan, R. 1998, ApJL, 497, L17
Sato, Y., Murase, K., Ohira, Y., Inoue, S., & Yamazaki, R. 2025, JHEAp, 48, 100415
Schroeder, G., Perley, D., & Laskar, T. 2026, GCN, 44235, 1
Sheth, K., Frail, D. A., White, S., et al. 2003, ApJL, 595, L33
Skrutskie, M. F., et al. 2006, AJ, 131, 1163
Soderberg, A. M., Kulkarni, S. R., Nakar, E., et al. 2006, Natur, 442, 1014
Stein, R., Mo, G., Karambelkar, V., et al. 2026, GCN, 43996, 1
Stratta, G., Fiore, F., Antonelli, L. A., Piro, L., & De Pasquale, M. 2004, ApJ, 608, 846
Sun, H., Li, W.-X., Liu, L.-D., et al. 2025, NatAs, 9, 1073
Tonry, J. L., Denneau, L., Flewelling, H., et al. 2018, ApJ, 867, 105
Troja, E., Piro, L., van Eerten, H., et al. 2017, Natur, 551, 71
Troja, E., Piro, L., Ryan, G., et al. 2018a, MNRAS, 478, L18
Troja, E., Ryan, G., Piro, L., et al. 2018b, NatCo, 9, 4089
Troja, E., van Eerten, H., Ryan, G., et al. 2019, MNRAS, 489, 1919
Troja, E., van Eerten, H., Zhang, B., et al. 2020, MNRAS, 498, 5643
Troja, E., Fryer, C. L., O'Connor, B., et al. 2022, Natur, 612, 228
Ulanov, M. V., Golenetskii, S. V., Frederiks, D. D., et al. 2005, NCimC, 28, 351
Urrutia, G., De Colle, F., Murguia-Berthier, A., & Ramirez-Ruiz, E. 2021, MNRAS, 503, 4363
Usov, V. V. 1992, Natur, 357, 472
van Eerten, H., & MacFadyen, A. 2013, ApJ, 767, 141
van Paradijs, J., Groot, P. J., Galama, T., et al. 1997, Natur, 386, 686
Virgili, F. J., Liang, E.-W., & Zhang, B. 2009, MNRAS, 392, 91
Virtanen, P., Gommers, R., Oliphant, T. E., et al. 2020, NatMe, 17, 261
Štrobl, J., Jelínek, M., & Hudec, R. 2019, AN, 340, 633
Štrobl, J., Jelínek, M., Polášek, C., & Hudec, R. 2023, CoSka, 53, 49
Wang, Y., Chen, C., & Zhang, B. 2026, JHEAp, 50, 100490
Waratkar, G., Kammoun, E., Jayaraman, R., Hinds, K.-R., & Ho, A. Y. Q. 2026, GCN, 44278, 1
Wardle, J. F. C., & Kronberg, P. P. 1974, ApJ, 194, 249
Wijers, R. A. M. J., & Galama, T. J. 1999, ApJ, 523, 177
Williams, M. A., Kennea, J. A., Dichiara, S., et al. 2023, ApJL, 946, L24
Willingale, R., Starling, R. L. C., Beardmore, A. P., Tanvir, N. R., & O'Brien, P. T. 2013, MNRAS, 431, 394
Wilms, J., Allen, A., & McCray, R. 2000, ApJ, 542, 914
Xu, F., Huang, Y.-F., Geng, J.-J., et al. 2023, A&A, 673, A20
Yadav, M., Troja, E., Ricci, R., et al. 2025, ApJ, 995, 216
Yamazaki, R., Yonetoku, D., & Nakamura, T. 2003, ApJL, 594, L79
Yang, J., Ai, S., Zhang, B.-B., et al. 2022, Natur, 612, 232
Yang, Y.-H., Troja, E., Yin, Y.-H.I., et al. 2026, GCN, 44375, 1
Yang, Y.-H., Troja, E., O'Connor, B., et al. 2024, Natur, 626, 742
Zhang, B., Kobayashi, S., & Mészáros, P. 2003, ApJ, 595, 950
Zhang, B., & Mészáros, P. 2002a, ApJ, 571, 876
Zhang, B., & Mészáros, P. 2002b, ApJ, 581, 1236
Zhang, B., & Mészáros, P. 2004, IJMPA, 19, 2385
Zhang, B., Zhang, B.-B., Virgili, F. J., et al. 2009, ApJ, 703, 1696
Zhang, B.-B., Zhang, B., Sun, H., et al. 2018a, NatCo, 9, 447
Zhang, B.-B., Zhang, B., Castro-Tirado, A. J., et al. 2018b, NatAs, 2, 69
Zheng, J.-H., & Lu, W. 2026, ApJL, 1003, L19
Zheng, J.-H., Zhu, J.-P., Lu, W., & Zhang, B. 2025, ApJ, 985, 21